TÉCNICO LISBOA

Performance Prediction of Floating Offshore Wind Turbines at Model- and Full-Scale with a RANS method

Álvaro Garrido Vital

Thesis to obtain the Master of Science Degree in

Mestrado Integrado em Engenharia Aeroespacial

Supervisors: Dr. João Manuel Ribeiro Costa Baltazar
Dr. Guilherme Vaz

Examination Committee

Chairperson: Prof. Afzal Suleman
Members of the Committee: Prof. João Manuel Melo de Sousa
Prof. Miguel Pérez-Saborid
Dr. João Manuel Ribeiro Costa Baltazar

October 2021

Acknowledgments

The work presented in this thesis is the final step in order to achieve the Double Master's Degree in Aerospace Engineering thanks to the collaboration between the Instituto Superior Técnico (IST) in Lisbon and the University of Seville (US). It is the result of several months of hard work with the support of WavEC Offshore Renewables and the Instituto Superior Técnico. Without their guidance, the study performed in this work would have been impossible and I want to use this lines to express my gratitude towards the following people.

Dr. Guilherme Vaz, who opened me the doors of WavEC despite the difficult health situation, allowed me to know great professionals during my stay there and gave me access to the computer power of the company. He always was willing to help me and supervised the progress of my study giving priceless suggestions.

João Manuel Ribeiro Costa Baltazar, member of the IST community and one of the most important helping hands during this period. I could count on him whenever I need despite his busy schedule.

Manuel Rentschler, employee of WavEC and the person who has giving me more time during the study, sharing with me his knowledge and love for numerical simulations.

Finally, I would like to thank my family, my friends and my girlfriend for supporting me during the tough moments of this period.

Álvaro Garrido Vital

Abstract

Floating wind turbines are becoming fashionable within the Renewable Energy world. Numerical analysis is imperative in order to improve the Floating Offshore Wind Turbines designs. This type of wind turbines are affected by both aerodynamic and hydrodynamic loads and modelling the fully coupled response is highly complex. The complete simulation of a full-scale turbine under wind and waves using viscous-flow Computational Fluid Dynamics codes is still nowadays very costly. An alternative is to model the Floating Offshore Wind Turbine behaviour using a scaled turbine of smaller dimensions. One method is using Froude-scaling to model the loads and geometric similarity for the dimensions. However, with this methodology, aerodynamic loads are not scaled properly due to Reynolds dissimilitude that can cause mismatch of it in model- and full-scale turbine. In this work, the aerodynamic analysis of model- and full-scale NREL 5MW wind turbines is performed with a RANS (Reynolds Averaged Navier-Stokes) solver, leaving the hydrodynamic part and coupled analysis for future studies. A different behaviour is determined comparing the performance of both turbines, mainly due to the different Reynolds number that makes the flow fully turbulent at full-scale while for model-scale there is transition. This affects the performance of the model-scale turbine specially at the power coefficient, that drops drastically in comparison with the full-scale one. Focusing on the model-scale turbine, the analysis is made for different grid refinements, turbulence models and transition models performing a verification procedure of the results, obtaining large uncertainties on the power coefficient and mismatch with the experiments, that demonstrate the difficulty of capturing the real flow behaviour with a RANS method.

Keywords

Floating wind turbines, RANS, Scale effects, Turbulence models, Transition models

Resumo

As turbinas eólicas flutuantes estão a tornar-se moda no mundo das Energias Renováveis. A análise numérica é imperativa a fim de melhorar o projeto das turbinas eólicas flutuantes. Este tipo de turbinas eólicas é afectado tanto por cargas aerodinâmicas como hidrodinâmicas e a modelação da resposta totalmente acoplada é altamente complexa. A simulação completa de uma turbina à escala real sob a ação do vento e ondas utilizando códigos de mecânica de fluídos computacional para escoamentos viscosos é ainda hoje muito dispendiosa. Uma alternativa trata-se de modelar o comportamento da turbina eólica flutuante utilizando uma turbina à escala de dimensões mais reduzidas. Um método é utilizar a escala de Froude para modelar as cargas e a semelhança geométrica para as dimensões. No entanto, com esta metodologia, as cargas aerodinâmicas não são devidamente dimensionadas devido à dissimilitude do número de Reynolds que pode causar grandes diferenças na previsão entre a turbina à escala do modelo e à escala real. Neste trabalho, a análise aerodinâmica da turbina eólica NREL 5MW tanto à escala do modelo como à escala real é realizada com um método RANS (Reynolds Averaged Navier-Stokes), deixando a parte hidrodinâmica e a análise acoplada para estudos futuros. Um comportamento diferente é determinado quando comparado o desempenho à escala do modelo com a escala real, principalmente devido ao diferente número de Reynolds que torna o escoamento totalmente turbulento à escala real, enquanto que para a escala do modelo prevê-se transição. Este efeito afecta o desempenho da turbina à escala do modelo, especialmente para o coeficiente de potência, que cai drasticamente em comparação com a turbina à escala real. Centrando-se na turbina à escala do modelo, a análise é feita para diferentes níveis de refinamento da malha, utilizando modelos de turbulência e modelos de transição, tendo sido realizado um estudo de verificação dos resultados, onde se obtiveram grandes incertezas para o coeficiente de potência e grandes diferenças com os resultados experimentais, que demonstram a dificuldade em prever o escoamento real com um método RANS.

Palavras Chave

Turbinas Eólicas Flutuantes, RANS, Efeitos de Escala, Modelos de Turbulência, Modelos de Transição.

Contents

List of Figures

List of Tables

Acronyms

AFM	Absolute-Formulation
ALE-VMS	Arbitrary Lagrangian-Eulerian Variational Multiscale
BEM	Boundary Element Method
CDS	Central Difference Scheme
DDES	Delayed Detached Eddy Simulation
DS	Dynamic Stall
DU	Delf University
DUT	Delft University of Technology
ECN	Netherlands Energy Research Foundation
EWEA	European Wind Energy Association
FOWT	Floating Offshore Wind Turbine
IC/RAL	Imperial College/Rutherford Appleton Laboratory
IEA	International Energy Agency
LES	Large Eddy Simulation
MEXICO	Model Experiments in Controlled Conditions
MVG	Moving-Grid-Formulation
NACA	National Advisory Committee for Aeronautics
NREL	National Renewable Energy Lab
NS	Navier-Stokes

QUICK Quadratic Upstream Interpolation for Convective Kinematics

RANS Reynolds Averaged Navier-Stokes

RE Richardson extrapolation

RFM Relative-Formulation

RMS Root Mean Square

S-A Spalart-Allmaras

SIMPLE Semi Implicit Method for Pressure Linked Equation

SST Shear Stress Transport

UDS Upwind Difference Scheme

U-RANS Unsteady Reynolds Averaged Navier-Stokes

VLM Vortice Lattice Method

VSM Viscous Sublayer Model

List of Symbols

B	Body force vector (N)
D	Deformation tensor (-)
e_f	Eccentricity vector (-)
I	Identity matrix (-)
T	Stress tensor for Newtonian fluids (Nm^{-2})
V	Velocity vector (ms^{-1})
n	Outward normal unit vector (-)
A	Area (m^2)
c	Chord lenght/Speed of sound (m/ms^{-2})
C_p	Pressure coefficient (-)
C_d	Drag coefficient (-)
C_l	Lift coefficient (-)
C_P	Power coefficient (-)
C_T	Thrust coefficient (-)
c_i	Refined cell size (m)
C_i	Initial cell size (m)
D	Diameter/Drag force (m/N)
F_s	Safety factor for numerical uncertainty study (-)
Fr	Froude number (-)
g	Gravitational constant (ms^{-2})
h	Vertical distance (m)
k	Turbulence kinetic energy per unit mass (m^2s^{-2})
L	Characteristic lenght/Lift force (m/N)
L_2	RMS of the residuals of ϕ (-)
L_∞	Norm of maximum residuals of ϕ (-)
M	Moment (Nm)
N	Number of rotor blades (-)
n_i	Number of refinements (-)
n_p	Total number of grid cells (-)
P	Pressure (Nm^{-1})
q_ϕ	Source term in conservation equation (ϕs^{-1})
R	Resulting force/Blade tip radius (N/m)
r	Radius (m)
Re	Reynolds number (-)

S	Platform area (m^2)
St	Strouhal number (-)
Tu	Turbulence intensity (-)
U_ϕ	Numerical uncertainty (-)
U_{inp}	Input uncertainty (-)
V_{wind}	Wind velocity (ms^{-1})
X_{cr}	Critical value along airfoil surface (m)
y^+	Non dimensional-wall distance (-)
α	Angle of attack (deg)
α_f	Interpolation factor (-)
α_t	Time discretization related constant (-)
β	Blending coefficient (-)
Δt	Time step (s)
δ	Boundary layer thickness (m)
Γ	Diffusive coefficient in conservation equation (-)
γ	Intermittency (-)
λ	Scaling factor (-)
μ	Dinamic viscosity ($kgm^{-1}s^{-1}$)
μ_t	Turbulence viscosity ($kgm^{-1}s^{-1}$)
$\mu_{tr}ef$	Normalized turbulence viscosity (-)
Ω	Angular velocity (s^{-1})
ω	Turbulence dissipation rate (-)
ϕ	Numerical flow quantity (-)
ϕ_0	Estimation of the exact solution (-)
ϕ_i	Integral of local quantity for iterarion i (-)
ϕ_{exact}	Exact solution (-)
ρ	Mass density (kgm^{-3})
τ	Shear stress (Nm^2)
τ_w	Shear stress on surface (Nm^2)
ν	Auxiliary viscosity ($kgm^{-1}s^{-1}$)
ϵ	Turbulence dissipation/Estimated discretization error (m^2s^{-2}/-)
res_ϕ	Non-dimensional change of the residual of a given variable (-)

1

Introduction

Contents

1.1 Motivation

The world population is increasing constantly year by year and in consequence there is a growing demand of energy worldwide. Fossil fuels prices increase is dropping the demand and giving a room for the development of clean and sustainable alternatives [1, 2]. One of the most widespread alternatives for clean and sustainable energy is wind. At the end of 2019, the total capacity for wind energy globally was over 651 GW, an increase of 10 % compared to 2018, and it is expected to grow over 355 GW in the next 4 years [3]. In 2005, a study of the potential wind energy generated worldwide was performed and it gave an estimation of 72 TW, which is more than enough to supply the energy needs of the world population [4].

Onshore wind energy technology has already been used with success in the last decades, with plenty of wind farms deployed worldwide, but it has lots of limitations. During the last years, a next step has been taken with the foundation of offshore wind installations, with a number of advantages.

The size of the onshore wind turbines is extremely limited by the transportation and erection equipment available, which constrains the amount of power obtained from the wind. On offshore wind turbines, the size of the wind turbines can be higher, thanks to the lifting capacities of marine shipping and handling equipment. The visual appearance of massive onshore wind turbine farms in populated areas are starting to be undesirable. This visual impact is mitigated by offshore turbines at a sufficient distance from the coast. Noise reduction, which increase the cost of onshore wind turbines, does not need so much attention on offshore wind turbines. Another advantage of offshore wind turbines is that the wind tends to blow faster and more uniformly at sea than on land due to the lack of topographical constraints such as mountains or buildings. This translates into less wear on the turbine components and more electricity generated per square meter of swept rotor area. Finally, onshore wind farms are usually located in remote areas, which needs the installation of long power lines to transmit the electricity to the populated areas, but offshore wind turbines can be placed close to high-value urban load centers.

The main disadvantage of the offshore wind turbines compared to the onshore ones is the increase in cost due to the higher investment costs and the restricted accessibility at sea, which translates into higher maintenance costs. Furthermore, the construction is technologically complicated and the environmental conditions at sea are more severe, more corrosion due to salt water and more loads from waves and ice, current loads, earthquakes, temperature variation, sea-bed movement and marine growth.

Despite this disadvantages, offshore wind turbines are currently the more promising way of wind energy extraction, although it is a technological challenge [5].

During the last decades, bottom-founded offshore wind installations have been working with success, bringing total cumulative installations to 29.1 GW at the end of 2019, 6.1 GW more than at the end of 2018. Furthermore offshore wind energy is not expected to be affected by the COVID-19 pandemic and will be the key for Green Recovery [6].

The water-depth is a limiting factor as the installation of very large wind turbines for really deep water increases significantly the cost. The next step after the bottom-founded offshore wind turbines are the Floating Offshore Wind Turbines (FOWTs), that consists in installing the wind turbines on top of a floating structure.

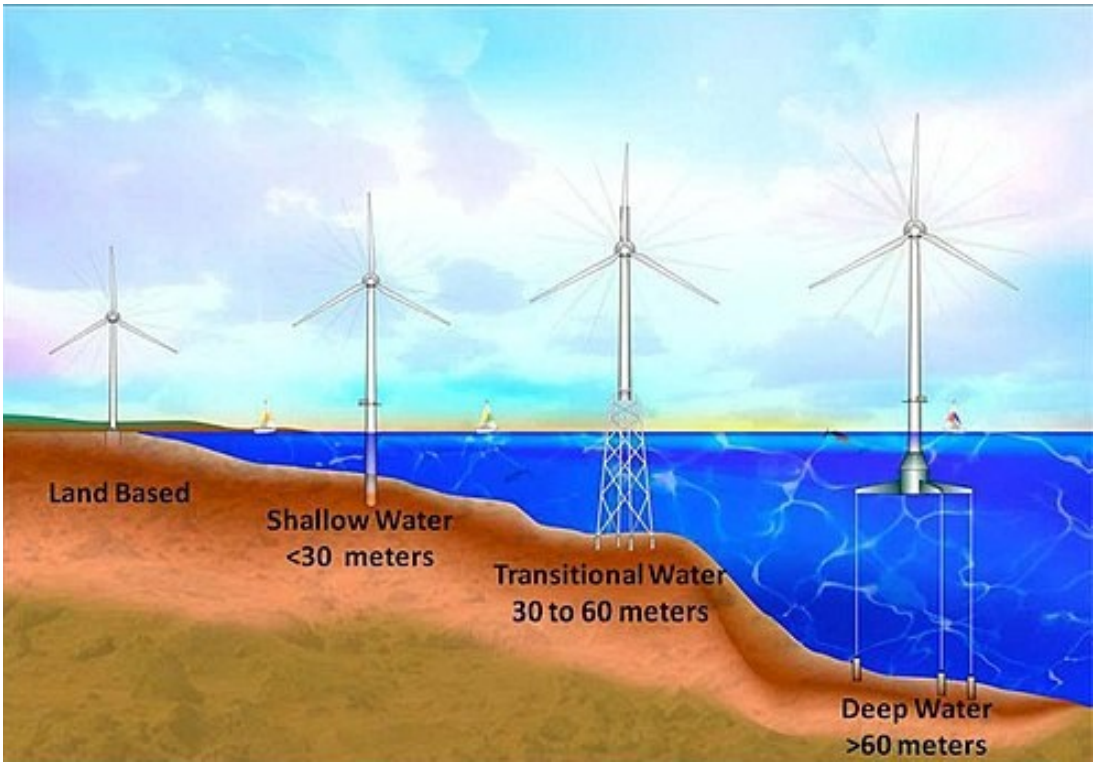

Figure 1.1: Technological evolution of wind turbine installations [7]

A report made by European Wind Energy Association (EWEA) stated that reliable FOWTs installations are necessary to unlock all the market potential in the Atlantic, Mediterranean and deep North Sea waters. It is stated that the potential wind energy that could be obtained on the deep waters of the North Sea could meet the total European Union electricity by four times [8]. Comparable statements were made by the National Renewable Energy Lab (NREL) for United States [9] All this statements seem very positive, but the deployment of the FOWTs installations is still on its first stages and the sector must

overcome technical, economic and political challenges. Both EWEA and NREL reports also state that reliable modeling tools are crucial for further improvement of FOWT designs.

In the past years several FOWTs design concepts have been investigated (see fig. 1.2). Moreover, some FOWTs installations have been deployed like the Hywind spar-buoy in Norway with a 2.3 MW turbine; the WindFloat in Portugal with a 2MW wind turbine; the Goto Island Project with a 2MW wind turbine in Japan [10]; or the VolturnUS 1:8 in US with a one-to-eight scale FOWT [11]. This last design was based on the NREL 5MW baseline turbine, the subject of study in this thesis. All this installations where just formed by one wind turbine. At the moment, just two FOWTs farms are operational, the Hywind Scotland and the WindFloat Atlantic. The first one was deployed in 2018 and it consists of 5 wind turbines that can give 30 GW of energy [12]. The second one was deployed in Portugal in 2020 and it consists of 3 wind turbines that can give 25 GW [13].

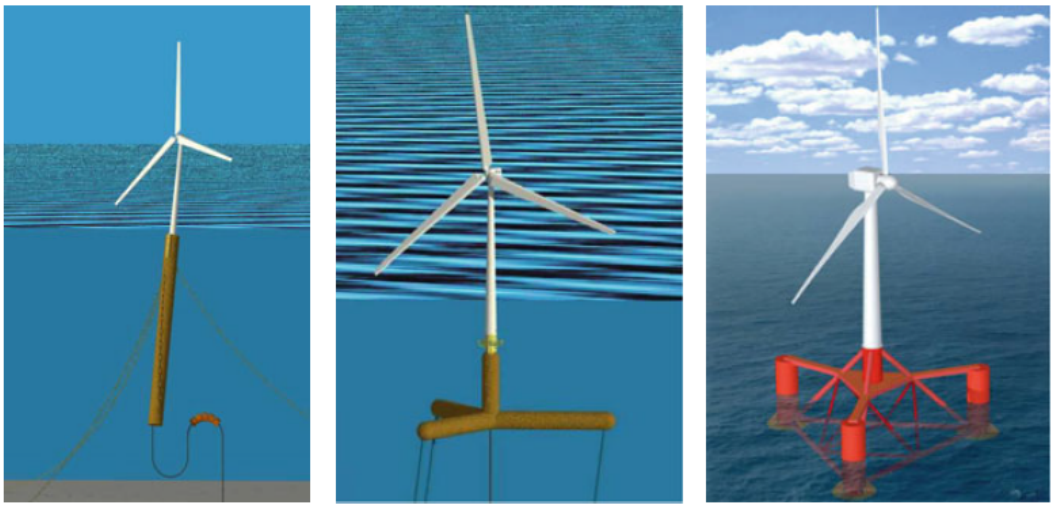

Figure 1.2: Support structure classes [10]

The FOWTs has several technical challenges as these turbines are exposed to more loads than the land based ones. There are additional loads such as irregular wave loads, ice loads, collision impact, ocean currents and many others (see fig. 1.3). In addition, fluid structure interaction has an important role due to the large and slender bodies (blades and tower) of these installations. Modeling the fully coupled aeroelastic and hydrodynamic response is therefore highly complex [14].

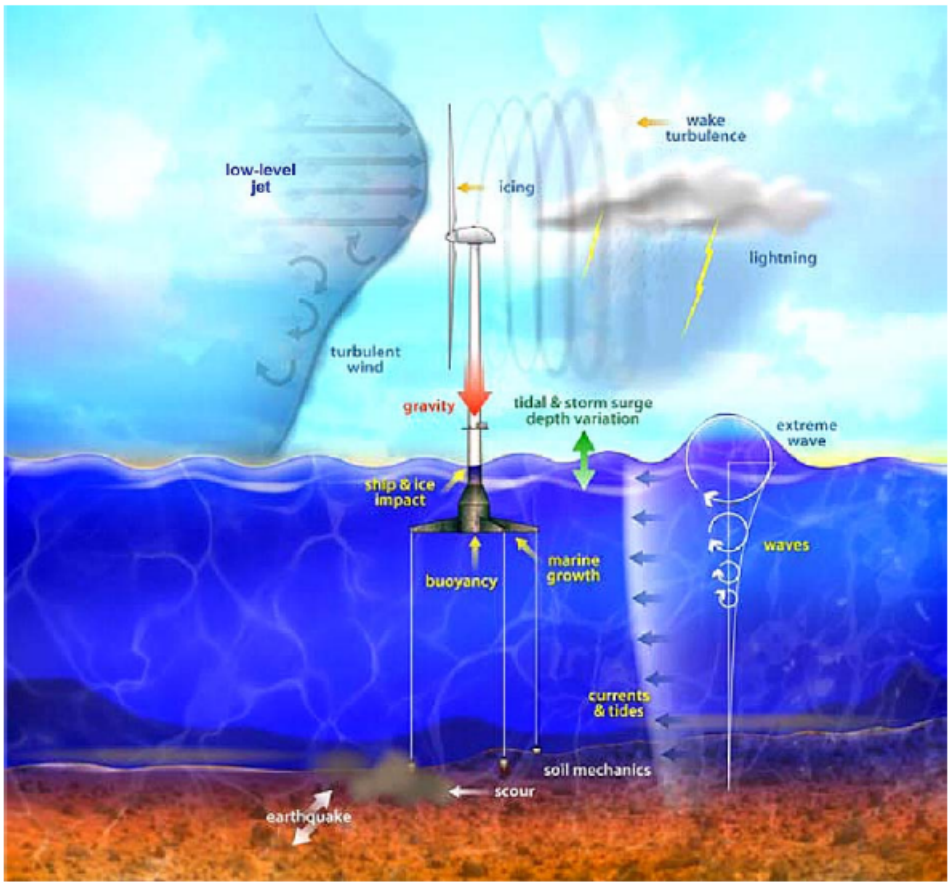

Figure 1.3: Environmental loads working on FOWTs [14]

1.2 Literature review

Experimental campaigns are crucial to validate the FOWT design tools and to better understand the complex underlying physics. During the last decades, several experimental campaigns have been performed on wind turbines (see table 1.1). Between these campaigns, there are three that should be highlighted. The NREL campaign, that took part on the United States from 1992 to 2001 and was divided in 6 phases of data recollection where two different turbines were tested. From this campaign, plenty of useful aerodynamic data was recollected. Also NREL tested a 1/50 model NREL 5MW turbine, the one studied on this thesis. Also important to highlight the European campaign performed by the International Energy Agency (IEA) with four campaigns carried out by differents institutions: Delft University of Technology (DUT), Imperial College/Rutherford Appleton Laboratory (IC/RAL), RISO laboratory and Netherlands Energy Research Foundation (ECN). Other important experimental campaign is the one performed in Netherlands, the Model Experiments in Controlled Conditions (MEXICO) campaign from 2007 to 2014 where considerable data was collected for different environmental and turbine conditions.

Table 1.1: Wind turbines experimental campaigns

Campaign (year)	Model	Data obtained	References
NREL phase I-IV (1992-1999)	Three bladed 10 m diameter	Complete measurement of all interesting aerodynamic data	[15, 16]
NREL phase V and VI (2001)	Two bladed 9.8 m diameter	Complete measurement of all interesting aerodynamic data	[17, 18]
MEXICO (2007)	Three bladed 4.5 m diameter rotor	Pressure and load for different V_w and TSR. PIV measurements	[19]
ECN (1993-1997)	Two bladed 27.44 m diameter rotor	Pressure distributions, normal and tangential forces, inflow velocities, angle of attack	[20]
IC/RAL (1997)	Three bladed 17 m diameter rotor	Pressure distributions, normal and tangential forces, inflow velocities, angle of attack	[20]
RISØ (1991-1993)	Three bladed 19 m diameter rotor	Pressure distributions, normal and tangencial forces, inflow velocities, angle of attack	[20]
DUT (1997)	Two bladed 10 m rotor diameter	Pressure distributions, normal and tangencial forces, inflow velocities, angle of attack	[20]
FINO 2 (2019)	Alpha Ventus wind farm (AV4 and AV5)	Power and tower bottom loads	[21]
MSWT (2014)	Three bladed 2.52 m diameter rotor	Trust and power for different TSR	[22]
NREL 5MW	Three bladed 2.56 m diameter rotor	Trust and power for different TSR	[23]
New MEXICO (2008-2014)	Three bladed 4.5 m diameter rotor	Pressure and load for different V_w and TSR. PIV measurements	[24]
NTNU	Three bladed 0.45 m diameter rotor	Thrust, power and wake	[25]
UNAFLOW (2018)	DTU 10MW	Thrust, power, wake and PIV measurements	[26]

As well as the experimental campaigns, it is also really important to perform numerical analysis in order to optimize the wind turbines and help for the design of them. In addition, they are a lot cheaper than experimental campaigns. Lots of numerical studies have been performed in the last years with different turbulence models and transition models. A summary of some significant studies are presented on table 1.2. Different numerical models have been used to predict the aerodynamic performance of wind turbines as potential flow models like Boundary Element Method (BEM) or Vortice Lattice Method (VLM) for the NREL 5MW wind turbine and MEXICO turbine respectively; Reynolds Averaged Navier-Stokes (RANS) and Unsteady Reynolds Averaged Navier-Stokes (U-RANS) models for NREL MW turbine and NREL Phase VI turbine with different turbulence models like $k-\omega$ SST model and Spalart-Allmaras (S-A) model. Some new studies have been performed with transitional models as the $\gamma - Re_\theta$ model. Also, more sophisticated models like Large Eddy Simulation (LES), Delayed Detached Eddy Simulation (DDES) or Arbitrary Lagrangian-Eulerian Variational Multiscale (ALE-VMS) have been used for the NREL 5MW turbine or the Beddoes-Leishman Dynamic Stall (DS) for the MEXICO turbine. Important to highlight the numerical study made my M. Make and G. Vaz on 2014 about the NREL 5 MW

wind turbine [23], that will be use as an starting point for the current thesis, where they used a RANS numerical method with a $k-\omega$ SST turbulence model to predict the aerodynamic behaviour of the wind turbine.

Table 1.2: Wind turbines numerical studies

Wind turbine	Numerical model	Turbulence/Transition Model	References
NREL 5MW	RANS	$K-\omega$ SST	[23]
	DDES	S-A (wall) and LES (rest)	[27]
	VLM	-	[28]
MSWT	RANS-BEMT	$K-\omega$ SST	[29]
	RANS	$K-\omega$ SST	[23]
MEXICO	RANS	$K-\omega$ SST	[30]
	BEM	-	[30]
	Multilevel Panel Method	-	[31]
	Beddoes-Leishman DS	-	[32]
Two back-to-back NREL 5MW	ALE-VMS	LES	[33]
	RANS	LES	[34]
VAWTs	U-RANS	$K-\omega$ SST	[35]
		S-A	
	DES	S-A	
NREL phase VI	U-RANS	$K-\omega$ SST	[36]
	RANS	$K-\omega$ SST	[37]
		$k-\omega$ SST/$\gamma-Re_\theta$	[38]

1.3 Objectives

The aim of the thesis is to perform a numerical analysis of the NREL 5MW wind turbine, a turbine designed for FOWTs applications, both model- and full-scale using a RANS CFD solver. The thesis will focus on the aerodynamic analysis, leaving the hydrodynamic part and coupled analysis for future studies.

The tasks of the thesis can be summarized as follows:

1. The research previously done by M. Make and G. Vaz will be evaluated to be used as a starting point for the .current thesis work.
2. A numerical study of the full-scale NREL 5MW using a RANS solver and a turbulence model focusing on the thrust and power coefficients for different TSR. This study will be compare with the previous study of M. Make and G. Vaz.
3. To further understand the aerodynamic behaviour of the full-scale NREL 5 MW, it will be also studied the friction and pressure coefficients for the design TSR ($TSR = 7$) as well as the limiting

streamlines calculation.

4. A numerical study considering the model-scale NREL 5 MW using a RANS solver and a turbulence model focusing on the thrust and pressure coefficients for different TSR. This study will be compared with the previous study of M. Make and G. Vaz and experimental results.
5. Numerical sensitivity analysis using different turbulence models and refinement sensitivity analysis for the design TSR on the NREL 5MW model-scale. Furthermore, a V & V study is performed to validate the numerical results against experimental measurement data.
6. To further understand the aerodynamic behaviour of the model-scale NREL 5 MW, the friction and pressure coefficients for the design TSR ($TSR = 7$) as well as limiting streamline calculation will also be studied.
7. Research on the use of a transition model to predict the aerodynamic behaviour of the model-scale NREL 5 MW.
8. Comparison of the aerodynamic behaviour of the NREL 5 MW at model-scale and full-scale.

1.4 Report summary

The remaining chapters of this report will provide a detailed description of the study and the relevant theory.

In chapter 2, the theory needed to understand the study will be presented. Topics such as the turbine aerodynamics or governing equations will be covered.

In chapter 3, the numerical background will be discussed, given information about the numerical tool and grid generation software used: ReFRESCO and Hexpress respectively.

The numerical setup used for the calculations is explained in chapter 4. The domain, boundary conditions or grid topology selected for the numerical study will be discussed.

In chapter 5, all the results obtained during this thesis will be presented, both for full-scale and model-scale NREL 5 MW.

Finally, an overall conclusion and recommendations regarding the complete study are provided in chapter 6.

2

Theory

Contents

2.1 Turbine Geometry and coordinates system

In this section, the geometry of the "NREL 5MW offshore baseline wind turbine" will be described and additionally, the respective coordinate system will be explained.

2.1.1 NREL 5MW baseline wind turbine geometry

The "NREL 5MW offshore baseline wind turbine" is a representative utility-scale multimegawatt wind turbine. This wind turbine was developed in support of concept studies which are aimed at assessing offshore wind technology and it is a conventional three-bladed upwind variable-speed variable blade-pitch-to-feather controlled turbine.

The NREL 5MW model is now commonly used as a reference by research teams throughout the world [39]. On table 2.1 the more relevant geometry and performance parameters for both full-scale and model-scale are presented, where the model-scale is scaled using Froude scaling and geometric similarity, with scaling parameter of $\lambda = 50$. This scaling methodology will be described on section 2.2.

Table 2.1: Properties of the full-scale and model-scale NREL 5MW baseline wind turbine [39]

Property	Full-scale	Model-scale	Units
Rated power	5	5.7	$[MW]/[W]$
Rotor diameter	126	2.52	$[m]$
Hub diameter	3	-	$[m]$
Hub height	90	1.80	$[m]$
Reynolds no. @ 0.7 Radius	11.5 $\times 10^6$	35.7 $\times 10^3$	$[-]$

The geometry of the blades is described on tables 2.2 and 2.3.

Table 2.2: Airfoil schedule [39]

Airfoil designation	Thickness (t/c)	Begin Radius (m)	End Radius (m)
Cylinder1	100%	1.8	5.98
Cylinder2	100%	5.98	10.15
DU40-A17	40.5%	10.15	15
DU35-A17	35.09%	15	20.49
DU30-A17	30%	20.49	26.79
DU25-A17	25%	26.79	34.22
DU21-A17	21%	34.22	42.47
NACA64-A17	18%	42.47	61.5

The blades are formed by different airfoils. The two innermost airfoil represent cylinders with drag coefficients of 0.50 (Cylinder1) and 0.35 (Cylinder2) and no lift. After that, the blade is formed by five airfoils from Delf University (DU) and one from National Advisory Committee for Aeronautics (NACA). The variables t and c on table 2.2 represent the thickness and the chord of the airfoil respectively.

Table 2.3: NREL 5MW chord and twist distribution [39]

RNodes (m)	DNodes	AeroTwst (deg)	Chord (m)
2.8667	2.733	13.308	3.542
5.6	2.733	13.308	3.854
8.3333	2.733	13.308	4.167
11.75	4.100	13.308	4.557
15.85	4.100	11.48	4.652
19.95	4.100	10.162	4.458
24.05	4.100	9.011	4.249
28.15	4.100	7.795	4.007
32.25	4.100	6.544	3.748
36.35	4.100	5.361	3.502
40.45	4.100	4.188	3.256
44.55	4.100	3.125	3.01
48.65	4.100	2.319	2.764
52.75	4.100	1.526	2.518
56.1667	2.733	0.863	2.313
58.9	2.733	0.37	2.086
61.6333	2.733	0.106	1.419

The blade node locations, labeled as “RNodes”, are directed along the blade-pitch axis from the rotor center to the blade cross sections. The element lengths, “DRNodes,” sum to the total blade length of 61.5 m. The aerodynamic twist, is labeled as “AeroTwst”.

2.1.2 Coordinate system

The coordinate system used in this study is a Cartesian coordinate system. The origin of the system is located at the intersection of the rotation axis and the swept plane of the rotor. The x-axis is pointing in the opposite direction to the wind direction, while the z-axis is pointing in the vertical upward direction. Finally, the y-axis is pointing in the horizontal direction resulting in a positive Cartesian coordinate system, as shown in fig. 2.1. In this figure also the wind velocity and the rotational direction of the turbine is indicated by vectors V_{wind} and Ω respectively.

2.2 Scaling methodology

Experiments are usually performed on model-scale wind turbines where the results should resemble the full-scale one. In order to achieve that, it is really important to properly scale the dynamic environment and behaviour of the system considered. The methodology applied by MARIN in previous tests will be used in this thesis [40] and it will be briefly described. This method is the one used because satisfactory results where obtained in previously studies performed by MARIN, who has a great experience in the

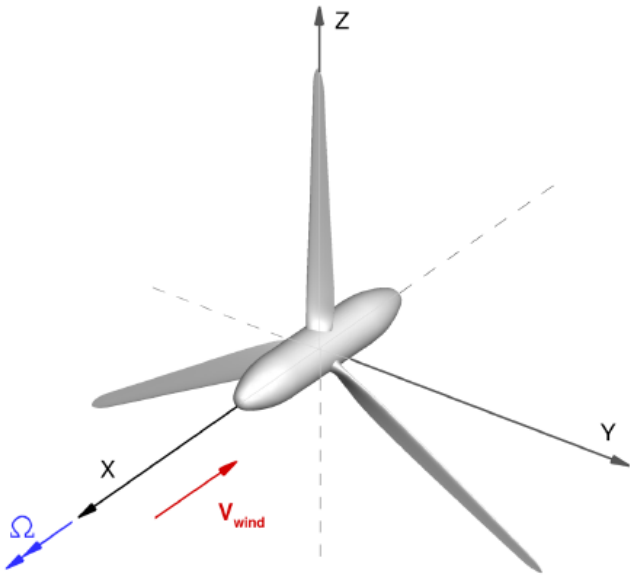

Figure 2.1: Coordinate system for the NREL 5 MW baseline wind turbine [23]

floating offshore wind turbine industry.

First of all, model-scale wing turbine will be scaled using Froude's scaling law in combination with geometric similarity. The Froude number, Fr, is a dimensionless parameter that quantifies the ratio between gravitational and inertial forces. This method is the most appropriate one for free and moored floating structure tests, since the gravitational effect of the water with a free surface predominates. The effects of other factors, such as viscosity and surface tension are often small such that they can be neglected [41].

Froude number is defined in eq. (2.1), where V represents the characteristic velocity, g the gravitational constant and L the characteristic dimension.

$$Fr = \frac{V}{\sqrt{gL}} \tag{2.1}$$

With Froude scaling method, Froude numbers of the full-scale turbine and model-scale turbine are equalized and with the geometrical similarity using the scaling factor $\lambda = L_f/L_m$, where the subscripts f and m represent the full-scale and model-scale wind turbine respectively, the velocity the wind should have on the model-scale experiment to have a similar dynamic environment as the full-scale one can be obtained.

By implementing Froude scaling most properties of interest, which influence the global dynamic response of the system, are scaled accurately, except for the aerodynamic wind loads, as will be discussed later [40].

The tip speed ratio, TSR is the ratio between the angular velocity multiplied by the radius of the turbine rotor and the inflow wind velocity. It is defined in eq. (2.2), where R the blade tip radius of the rotor and V_wind the wind inflow velocity [42].

$$TSR = \frac{\Omega R}{V_{wind}} \tag{2.2}$$

Maintaining the same TSR between model-scale and full-scale turbine will ensure that the rotational speed and the corresponding excitation frequencies caused by aerodynamic effects are scaled correctly.

As it was said before, the aerodynamic loads are not scaled accurately with Froude scaling, this is due to complications with the Reynolds number that can cause mismatch of it in model and prototype. The Reynolds number, Re, is a dimensionless parameter that quantifies the ratio of inertial forces to viscous forces within the fluid. Its definition is given in eq. (2.3) where ρ represents the density of the fluid, V the fluid velocity and μ the dynamic viscosity of the fluid.

$$Re = \frac{\rho V L}{\mu} \tag{2.3}$$

While Froude number is the primary scaling parameter in hydrodynamic model tests, the Reynolds number effects are not scaled properly for large scaling factors. When a model is Froude scaled, its Reynolds number will be $\lambda^{1.5}$ times smaller than the full-scale Reynolds number. The consequence of this is that the flow at full-scale can be fully turbulent while for the model-scale can be laminar. The effects on the aerodynamic performance will be discussed in section 2.3.2.

2.3 Turbine Aerodynamics

In this section, the aerodynamics of the turbine will be described base on a 2D airfoil. The airflow around the wind turbine is three dimensional, but part of the theory to describe the wind turbine performance relies mainly on two dimensional wing section data.

2.3.1 Forces acting on a airfoil

The aerodynamic performance is commonly described by three parameters: lift, drag and the moment generated by the airflow around a foil. The airflow creates a pressure P when acting on the airfoil. This pressure is perpendicular to it and is generated by the rate of change of momentum of the air molecules impacting on the airfoil surface. Additionally a shear stress τ tangential to the surface of the airfoil is generated due to the frictional property of the airfoil. The combination of this two forces generates a momentum M and resultant force R. This is represent in fig. 2.2.

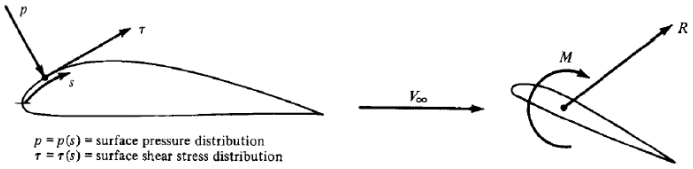

Figure 2.2: Forces acting on an airfoil [43]

This force R is decomposed in two forces: one perpendicular to the airflow direction called lift L and other parallel to the airflow direction called drag D. This decomposition is represented in fig. 2.3. The lift force is dominated by pressure contributions while drag is dominated by frictional forces.

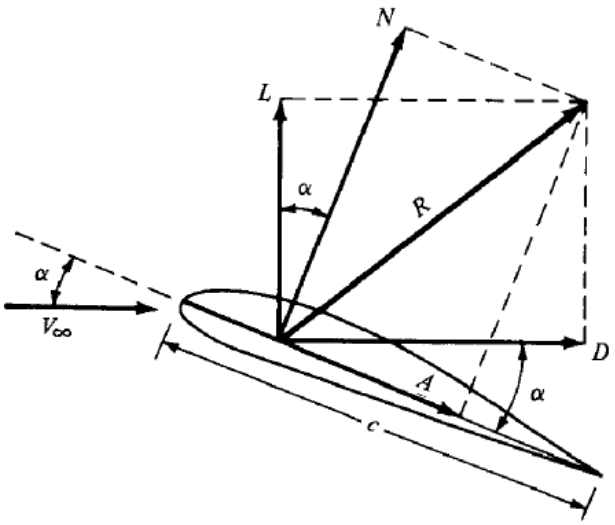

Figure 2.3: Decomposition of resultant force [43]

Lift and drag as well as the moment can be non-dimensionalized using a reference area S, a reference lenght l and the free-stream dynamic pressure which is given by eq. (2.4), where the subscript ∞ represents the properties of the flow far upstream.

$$q_\infty \equiv \frac{1}{2}\rho_\infty V_\infty^2 \tag{2.4}$$

The resulting dimensionless coefficients of lift, drag and moment are given in equations eqs. (2.5) to (2.7).

$$C_L \equiv \frac{L}{q_\infty S} \tag{2.5}$$

$$C_D \equiv \frac{D}{q_\infty S} \tag{2.6}$$

$$C_M \equiv \frac{M}{q_\infty S l} \tag{2.7}$$

These expressions are valid for three-dimensional airfoils. The efficiency of an airfoil is commonly represent with the drag to lift ratio as can be seen in eq. (2.8).

$$\frac{L}{D} = \frac{q_\infty S C_L}{q_\infty S C_D} = \frac{C_L}{C_D} \tag{2.8}$$

Another coefficient usually used in airfoil aerodynamics is the pressure coefficient C_p that describes the pressure in a non-dimensional way. This is done by dividing the pressure by the dynamic pressure of the free-stream flow, as shown in eq. (2.9).

$$C_p = \frac{P - P_\infty}{q_\infty} \tag{2.9}$$

2.3.2 Boundary Layer

A really important part for the aerodynamics of an airfoil is the boundary layer. It is located close to the surface of the airfoil, where the viscous forces are relevant. The thickness of the boundary layer varies and the flow can be laminar or turbulent. When the boundary layer is laminar, the flow is smooth and regular while in turbulent boundary layer the flow moves randomly and irregular.

The difference in aerodynamic performance between laminar and turbulent boundary layers is huge. In fig. 2.4 it can be seen that the turbulent velocity profile is “fatter’, or fuller, than the laminar profile. The variable $\bar{u}$ represents the mean velocity of the flow. For the turbulent profile, from the outer edge to a point near the surface, the velocity remains reasonably close to the free-stream velocity; it then rapidly decreases to zero adjacent to the wall. In contrast, the laminar velocity profile gradually decreases to zero from the outer edge to the surface. The velocity gradients and frictional forces are higher when the boundary layer is turbulent.

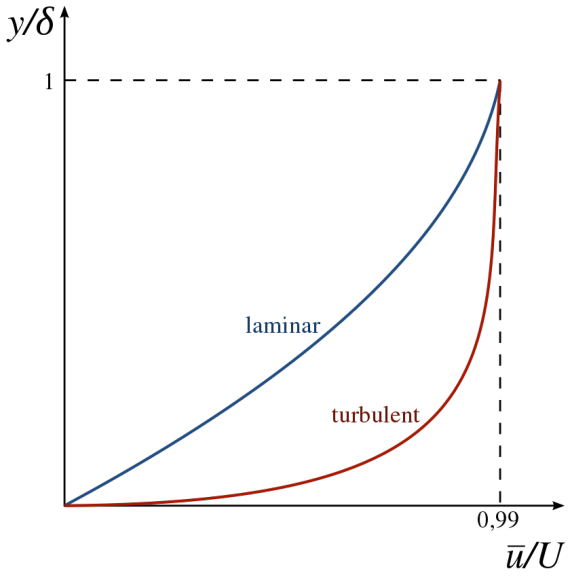

Figure 2.4: Velocity profiles of laminar and turbulent boundary layers

The change between laminar to turbulent flow is called transition. The point where the transition takes place depends on several variables, like the velocity of the flow or the roughness of the surface. The x_{cr} is the value of x along the airfoil surface where the transition takes place. This defines a critical Reynolds number, $Re_{x_{cr}}$, given in eq. (2.10).

$$Re_{X_{cr}} = \frac{\rho_\infty V_\infty x_{cr}}{\mu_\infty} \tag{2.10}$$

Using the Reynolds number and the boundary layer thickness, the skin-friction coefficient can be estimated based on flat-plate theory for both laminar and turbulent flow as given in eqs. (2.11) and (2.12) [43], where δ is the boundary layer thickness at a certain location x along the airfoil surface, Re_x the Reynolds number at location x from the leading edge of the surface.

$$C_{f_{lam}} \approx \frac{1.328}{\sqrt{Re}}, \quad \delta_{lam} \approx \frac{5.0x}{\sqrt{Re_x}} \tag{2.11}$$

$$C_{f_{turb}} \approx \frac{0.074}{Re^{1/5}}, \quad \delta_{turb} \approx \frac{0.37x}{Re_x^{1/5}} \tag{2.12}$$

When the velocity is decreasing in the flow direction, an adverse pressure gradient is produced, whose magnitude has a great influence on the boundary. Depending on the curvature of the airfoil, this increasing pressure gradient can result in a negative velocity in the boundary layer that can produce the separation of it as it is shown on fig. 2.5.

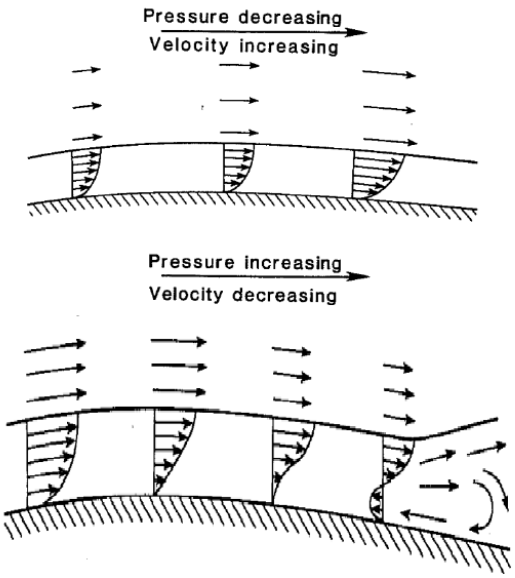

Figure 2.5: Effect of pressure gradients on the boundary layer [44]

As it was said before, the state of the boundary layer has a huge impact in the performance of the airfoil. Laminar boundary layer stability is affected by pressure gradients and Reynolds number. Depending on the Reynolds number, the laminar boundary layer reacts to pressure gradients in three different ways as can be seen in figure fig. 2.6.

2.4 Equations

In this section the equations that govern the viscous flows will be presented. The fluid is considered Newtonian, incompressible and isothermal. The fluid velocity is given by the vector $\mathbf{V} = (u, v, w)^T$,

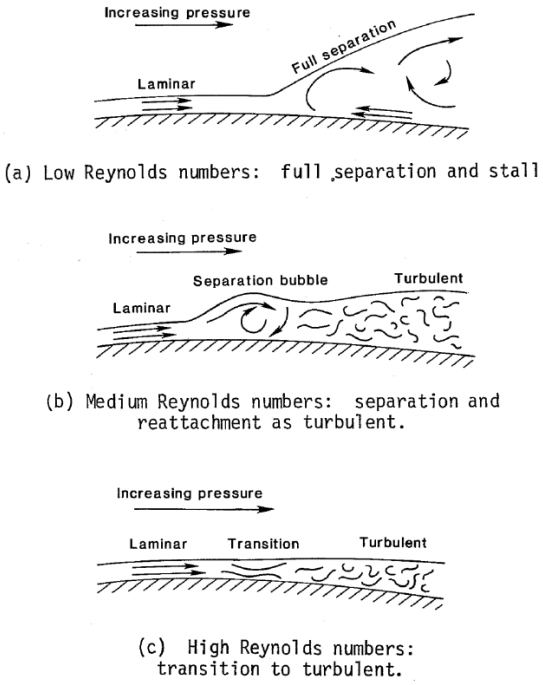

Figure 2.6: Reynolds number effects on laminar boundary layer subject to adverse pressure gradient [44]

where u, v and w are the Cartesian components of the velocity vector.The density, static pressure, and dynamic viscosity are denoted ρ, p and μ respectively. Additionally a fixed spatial Cartesian coordinate system is assumed in this section.

2.4.1 Navier-Stokes equations

Only the important equations and derivations of the Navier-Stokes (NS) equations are presented in this sections, for a full detailed derivation see [43].The Navier-Stokes (NS) equations consists of two equations: the conservation of mass equation and the momentum equation, that are presented on eqs. (2.13) and (2.14) respectively.

$$\frac{\partial \rho}{\partial t} + \nabla \cdot (\rho \mathbf{V}) = 0 \tag{2.13}$$

$$\frac{\partial (\rho \mathbf{V})}{\partial t} + \nabla \cdot (\rho \mathbf{V}\mathbf{V}) = \nabla \cdot \mathbf{T} + \rho \mathbf{B} \tag{2.14}$$

where $\mathbf{B}$ is the body force vector and $\mathbf{T}$ the stress tensor which is given by eq. (2.15),

$$\mathbf{T} = \left(p + \frac{2}{3}\mu\nabla\cdot\mathbf{V}\right)\mathbf{I} + 2\mu\mathbf{D} \tag{2.15}$$

where $\mathbf{I}$ is the identity matrix and $\mathbf{D}$ the deformation tensor given by eq. (2.16).

$$\mathbf{D} = \frac{1}{2}\left(\nabla\mathbf{V} + \nabla\mathbf{V}^T\right) \tag{2.16}$$

The flow is incompressible, which makes the density constant, so the mass conservation equation and the momentum equation can be written as,

$$\nabla\cdot\mathbf{V} = 0 \tag{2.17}$$

$$\rho\left(\frac{\partial\mathbf{V}}{\partial t} + \nabla\cdot(\mathbf{V}\mathbf{V})\right) = \nabla\cdot\mathbf{T} + \rho\mathbf{B} \tag{2.18}$$

The air is compressible, but for aerodynamics problems where the velocity is much lower than the speed of sound, the assumption of incompressible flow can be used. This assumption will be used in this thesis.

The fluid properties can be divided into a mean time dependant part and a fluctuating part, that for the x axis velocity component translates into eq. (2.19).

$$u_i = \overline{u_i}(x,y,z) + u_i'(x,y,z,t) \tag{2.19}$$

The mean and time fluctuating values have the properties shown in eq. (2.20).

$$\overline{u'} = 0, \quad \overline{\bar{u}} = \bar{u}, \quad \text{and} \quad \overline{\bar{f}\bar{g}} = \bar{f}\bar{g} \tag{2.20}$$

This method of decomposing flow quantities is used in the derivation of the RANS equations and is referred to as Reynolds decomposition, and can be graphically seen in figure fig. 2.7.

As was mentioned before, the flow around an object can have two different flow regions: a laminar and a turbulent region. In laminar flows, the perturbations are dampened by the viscous forces while on turbulent flows the viscous forces are not strong enough to dampen this perturbations and are dominated by inertial forces.

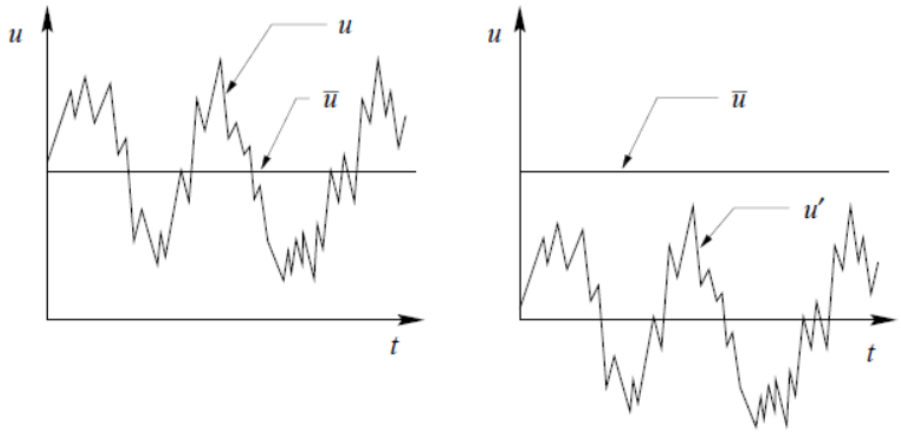

Figure 2.7: Reynolds decomposition in mean and time fluctuating values

Two ways of describing the turbulence of the fluid flow is by the turbulence intensity T_i and the turbulence kinetic energy per unit mass k that are defined in eqs. (2.21) and (2.22).

$$T_i = \frac{\sqrt{\frac{2}{3}k}}{\overline{\mathrm{V}}} \tag{2.21}$$

$$k = \frac{1}{2}\left(\overline{u'^2} + \overline{v'^2} + \overline{w'^2}\right) \tag{2.22}$$

The turbulence kinetic energy is characterized by the Root Mean Square (RMS) of the velocity fluctuations.

2.4.2 Reynolds-Averaged Navier-Stokes (RANS) equations

Simulating the turbulent flow using directly the NS equations requires very fine grids and time steps to properly model small perturbations present in the flow, which requires large amount of CPU power. In order to solve this, in many engineering problems it is enough to know the mean flow phenomena, so Reynolds decomposition is performed and the NS are converted in a more feasible model called the RANS equations. Applying the Reynolds decomposition to the mass conservation equation (eq. (2.13)), results in eq. (2.23).

$$\begin{aligned} \nabla \cdot \overline{\mathbf{V}} &= 0, \quad \text{and} \\ \nabla \cdot \mathbf{V}' &= 0 \end{aligned} \tag{2.23}$$

In the same way, the momentum conservation equation can be written as eq. (2.24).

$$\rho \frac{\partial \bar{V}_i}{\partial t} + \rho \frac{\partial \bar{V}_i \bar{V}_j}{\partial x_j} = \rho \bar{f}_i + \frac{\partial}{\partial x_j} \left[\bar{p} \delta_{ij} + \mu \left(\frac{\partial \bar{V}_i}{\partial x_j} + \frac{\partial \bar{V}_j}{\partial x_i} \right) - \rho \overline{V_i' V_j'} \right] \tag{2.24}$$

These equations are similar to the NS equations except for an extra set of terms in the momentum equation given by $\rho \overline{V_i' V_j'}$, which are known as the Reynolds stresses.

As we can see, there are four independent governing equations, three from the momentum conservation equations and one from the mass conservation equation. But there are more than four unknown variables. These are the mean velocities components $\overline{V}$, the mean pressure $\overline{p}$, and the Reynolds stresses. This set of equations is unclosed and cannot be solved [45]. To close the problem, a turbulence model is needed. Some turbulence models will be describe on section 2.4.3.

2.4.3 Turbulence models

As it was said before, in order to close the problem and solve the RANS equations a turbulence model is needed. There are many of them, but during these thesis just three of them will be used: Spalart-Allmaras, $k - \omega$ SST and KSKL turbulence models.

All this three models are based on the turbulence-viscosity hypothesis first introduced by Boussinesq in 1877 and has one or two equations depending on the number of turbulence quantities for which the model transport equations are solved. In this approach the Reynolds stresses are related to the mean rate of strain of a fluid element as shown in eq. (2.25).

$$-\rho \overline{V_i' V_j'} = \mu_t \left(\frac{\partial \bar{V}_i}{\partial x_j} + \frac{\partial \bar{V}_j}{\partial x_i} \right) - \frac{2}{3} \rho k \delta_{ij} \tag{2.25}$$

In this equation there is a new scalar μ_t called *turbulence viscosity* or *eddy viscosity*.

2.4.3.A Spalart-Allmaras model

This is a one-equation model that was developed for aerodynamics applications, and just solve a single transport equation to determine the turbulence viscosity μ_t. The S-A is a considerable improvement from the algebraic models (models that do not require the solution of any additional equation, and are calculated directly from the flow variables) and is a simple alternative to the two-equations models [45].

The SA defines the turbulence viscosity as the product of an auxiliary viscosity $\tilde{\nu}$ and an auxiliary function f_{v1} as presented in eq. (2.26).

$$\nu_t = \tilde{\nu} f_{v1} \tag{2.26}$$

In this expression ν_t is the kinematic turbulence viscosity $\nu_t = \mu_t/\rho$. The auxiliary viscosity $\tilde{\nu}$ follows the transport equation eq. (2.27).

$$\begin{aligned}\frac{\partial \rho\tilde{\nu}}{\partial t} + \underbrace{\frac{\partial}{\partial x_j}\left(\rho\tilde{\nu}U_j\right)}_{\text{Convection}} = &\underbrace{c_{b1}\left(1-f_{v1}\right)\rho\tilde{S}\tilde{\nu} + \cdots}_{\text{Production}} \\ &\underbrace{+\frac{1}{\sigma}\left\{\frac{\partial}{\partial x_j}\left[\rho(\nu+\tilde{\nu})\frac{\partial\tilde{v}}{\partial x_j}\right] + c_{b2}\rho\frac{\partial\tilde{\nu}}{x_j}\frac{\partial\tilde{\nu}}{x_j}\right\} + \cdots}_{\text{Diffusion}} \\ &\underbrace{-\left(c_{w1}f_w - \frac{c_{b1}}{\kappa^2}f_{t2}\right)\rho\left(\frac{\tilde{\nu}}{d}\right)^2}_{\text{Dissipation}}.\end{aligned} \tag{2.27}$$

The coefficients and auxiliary functions are based on basis models for shear flows, boundary layer flow models and transition flow models. The coefficients are as follows:

$$\begin{aligned} c_{b1} &= 0.1355, \quad c_{b2} = 0.622, \quad \sigma = \frac{2}{3}, \quad \kappa = 0.41 \\ c_{w1} &= \frac{c_{b1}}{\kappa^2} + \frac{1+c_{b2}}{\sigma}, \quad c_{w2} = 0.3, \quad c_{w3} = 2 \\ f_{t2} &= c_{t3}\exp\left(-c_{t3}\mathcal{X}^2\right), \quad c_{t3} = 1.2, \quad c_{t4} = 0.5 \\ r &= \min\left(10, \frac{\tilde{\nu}}{\tilde{S}\kappa^2 d^2}\right), \quad g = r + c_{w2}\left(r^6 - r\right), \quad f_w = g\left(\frac{1+c_{w3}^6}{g^6 + c_{w3}^6}\right)^{1/6} \end{aligned} \tag{2.28}$$

The auxiliary functions which are related to the flow close to walls are given by,

$$\begin{aligned} \tilde{S} = S + \frac{\tilde{\nu}}{\kappa^2 d^2}f_{v2}, \quad S = \sqrt{2S_{ij}S_{ji}}, \quad \mathcal{X} = \frac{\tilde{\nu}}{\nu} \\ f_{v1} = \frac{\mathcal{X}^3}{\mathcal{X}^3 + c_{v1}^3}, \quad f_{v2} = 1 - \frac{\mathcal{X}}{1+\mathcal{X}f_{v1}}, \quad c_{v1} = 7.1 \end{aligned} \tag{2.29}$$

A more detailed description of the Spalart-Allmaras model can be found in [46].

2.4.3.B $k-\omega$ SST model

Many two-equations methods have been proposed where the turbulence kinetic energy k is used as one of the variables and different choices for the second variable. One of the most widely used is the $k-\epsilon$ model [47]. This model uses the turbulence dissipation ϵ as the second variable. In the case of the $k-\omega$ model, the second variable used is the turbulence dissipation rate ω define as $\omega = \epsilon/k$. This model was first introduced by Wilcox [48].

The $k-\epsilon$ model performs well away from the walls while the $k-\omega$ model performs well near them. Menter combined this two models forming the $k-\omega$ Shear Stress Transport (SST) model, which is a blend between the $k-\epsilon$ model near walls, and $k-\omega$ model far from walls [49].

The model turbulence viscosity is given by eq. (2.30)

$$\mu_t = \frac{\rho k/\omega}{\max\left(1, \Omega F_2/\left(a_1\omega\right)\right)}, \quad \text{where } a_1 = 0.31 \tag{2.30}$$

In the previous equation, Ω represents the the magnitude of the vorticity defined as $\Omega = \sqrt{2\omega_{ij}\omega_{ij}}$. The auxiliary function F_2 is defined by eq. (2.31) where d is the wall distance.

$$F_2 = \tanh\left\{\left[\max\left(2\frac{\sqrt{k}}{0.09d\omega}, \frac{500\mu}{\rho d^2\omega}\right)\right]^2\right\} \tag{2.31}$$

The transport equations for the turbulence kinetic energy k and the turbulence dissipation rate ω are defined in eqs. (2.32) and (2.33) respectively.

$$\frac{\partial \rho k}{\partial t} + \frac{\partial}{\partial x_j}[\underbrace{\rho U_j k}_{\text{Convection}} \underbrace{- \mu + \sigma_k \mu_t)\frac{\partial k}{\partial x_j}}_{\text{Diffusion}}] = \underbrace{\tilde{P}}_{\text{Production}} - \underbrace{\beta^* \rho\omega k}_{\text{Destruction}} \tag{2.32}$$

$$\frac{\partial \omega \rho}{\partial t} + \frac{\partial}{\partial x_j}[\underbrace{\rho U_j \omega}_{\text{Convection}} \underbrace{- (\mu + \sigma_\omega \mu_t)\frac{\partial \omega}{\partial x_j}}_{\text{Diffusion}}] = \underbrace{\gamma\rho\tilde{P}}_{\text{Prod.}} - \underbrace{\beta\rho\omega^2}_{\text{Destr.}} + \underbrace{2\left(1 - F_1\right)\frac{\rho\sigma_{\omega 2}}{\omega}\frac{\partial k}{\partial x_j}\frac{\partial \omega}{\partial x_j}}_{\text{Blending}} \tag{2.33}$$

The auxiliary function F_1 is given by eq. (2.34).

$$F_1 = \tanh\left\{\left[\min\left[\max\left(2\frac{\sqrt{k}}{\beta^* d\omega}, \frac{500\mu}{\rho d^2\omega}\right), \frac{4\rho\sigma_{\omega 2}\kappa}{CD_{k\omega}d^2}\right]\right]^4\right\}, \tag{2.34}$$

where,

$$CD_{k\omega} = \max\left(\frac{2\rho\sigma_{\omega 2}}{\omega}\frac{\partial k}{\partial x_j}\frac{\partial \omega}{\partial x_j}, 10^{-20}\right), \quad \beta^* = 0.09, \quad \kappa = 0.41 \tag{2.35}$$

The production $\tilde{P}$ is limited to prevent the build-up of turbulence in stagnation regions:

$$\tilde{P} = \min\left(\tau_{ij}S_{ij}, 20 \cdot \beta^* \rho k\omega\right) \tag{2.36}$$

The remaining coefficients, β, γ, σ_k and σ_ω are defined by a blending between the coefficients of the original $k-\omega$ model and $k-\epsilon$ transformed model. Both models are denoted by 1 or 2 respectively. The blending of both constants is defined by,

$$\phi = F_1\phi_1 + (1 - F_1)\,\phi 2, \quad \phi = \{\beta, \gamma, \sigma_k, \sigma_\omega\} \tag{2.37}$$

The values of the coefficients are as follows,

$$\begin{array}{llll} \sigma_{k1} = 0.85, & \sigma_{\omega 1} = 0.50, & \beta_1 = 0.075, & \gamma_1 = \frac{\beta_1}{\beta^*} - \frac{\sigma_{\omega 1}\kappa^2}{\sqrt{\beta^*}} = 0.553 \\ \sigma_{k2} = 1.00, & \sigma_{\omega 2} = 0.856, & \beta_2 = 0.0828, & \gamma_2 = \frac{\beta_2}{\beta^*} - \frac{\sigma_{\omega 2}\kappa^2}{\sqrt{\beta^*}} = 0.440 \end{array} \tag{2.38}$$

After several years of experience, the $k-\omega$ SST model was slightly modified in 2003 [50]. The major change is that the strain rate S is used instead of the vorticity Ω. So $\Omega = \sqrt{2\omega_{ij}\omega_{ij}}$ is replaced by $S = \sqrt{2S_{ij}S_{ij}}$ and the resulting expression of the turbulence viscosity μ_t is converted into equation eq. (2.39).

$$\mu_t = \frac{\rho k/\omega}{\max\left(1, SF_2/\left(a_1\omega\right)\right)} \tag{2.39}$$

Additionally the limiter to prevent the build-up of turbulence in stagnation regions is altered where a factor 10 instead of 20 is used.

$$\tilde{P} = \min\left(\tau_{ij}S_{ij}, 10 \cdot \beta^* \rho k\omega\right) \tag{2.40}$$

This modified version of the initial $k-\omega$ SST model is the one used on this thesis.

2.4.3.C $k-\sqrt{k}L$ model

This two-equation model comes from the modelling concept proposed by Rotta [51], which uses an exact transport equation for the turbulent length scale L. Rotta proposed a $k-kL$ with a third derivative velocities, that was changed to a second derivative velocities as they offer a more attractive modelling

framework. Also it was formulated as a $k-\sqrt{k}L$ model due to practical considerations and a slightly superior performance. The major improvement of this model is the better performance for unsteady flows than other two-equations models proposed before as the $k-\omega$ SST model.

Assuming flows with a dominant shear strain normal to the inflow direction, the turbulent length scale L is defined in eq. (2.41).

$$kL = -cv_t \left|\frac{\partial U}{\partial y}\right|^2 L \left(\frac{L}{L_{vK}}\right)^2 \quad L_{vK} = \kappa \left|\frac{\partial U/\partial y}{\partial^2 U/\partial y^2}\right| \tag{2.41}$$

Changing the formulation from a kL form to a $\Phi = \sqrt{k}L$ form, the resulting two equation model is presented in eqs. (2.42) to (2.44).

$$\frac{\partial(\rho k)}{\partial t} + \frac{\partial\left(\rho U_j k\right)}{\partial x_j} = P_k - c_\mu^{3/4}\rho\frac{k^{3/2}}{L} + \frac{\partial}{\partial x_j}\left(\frac{\mu_t}{\sigma_k}\frac{\partial k}{\partial x_j}\right) \tag{2.42}$$

$$\frac{\partial(\rho\Phi)}{\partial t} + \frac{\partial\left(\rho U_j \Phi\right)}{\partial x_j} = \frac{\Phi}{k}P_k\left(\zeta_1 - \zeta_2\left(\frac{L}{L_{vK}}\right)^2\right) - \zeta_3\rho k + \frac{\partial}{\partial x_j}\left(\frac{\mu_t}{\sigma_\Phi}\frac{\partial\Phi}{\partial x_j}\right) \tag{2.43}$$

$$\frac{\mu_t}{\rho} = v_t = c_\mu^{1/4}\Phi; \quad P_k = \mu_t S^2; \quad S = \sqrt{2S_{ij}S_{ij}}; \quad S_{ij} = \frac{1}{2}\left(\frac{\partial U_i}{\partial x_j} + \frac{\partial U_j}{\partial x_i}\right) \tag{2.44}$$

The values of the model coefficients are as follows,

$$\begin{gathered} c_\mu = 0.99, \quad \kappa = 0.41, \quad \zeta_1 = 0.8, \quad \zeta_2 = 1.47 \\ \zeta_3 = 0.0288, \quad \sigma_k = 2/3, \quad \sigma_\Phi = 2/3 \end{gathered} \tag{2.45}$$

In order to be able to integrate the model to the viscous sublayer, additional near wall damping terms are required. The following Viscous Sublayer Model (VSM) terms are added to the right hand sides of the k and Ψ equations, respectively, where d is the distance to the nearest surface.

$$\begin{gathered} VSM_k = -2\mu\frac{k}{d^2}; \quad VSM_\Phi = -6\mu\frac{\Phi}{d^2}f_\Phi \\ f_\Phi = \frac{1+c_{d1}\xi}{1+\xi^4}; \quad \xi = \frac{\sqrt{0.3\cdot k}\cdot d}{20\cdot v}; \quad c_{d1} = 4.7 \end{gathered} \tag{2.46}$$

Turbulence models need additional adjustments to flow situations for which they have not been calibrated initially. In this case is for adverse pressure gradient regions and for stagnation regions. Both problems can be handled with one modification to the eddy viscosity, with different constants outside and inside the boundary layer. This modifications are presented in eq. (2.47).

$$\begin{aligned}
&\nu_t = \min\left(c_\mu^{1/4}\Phi,\, \tfrac{a_1 k}{S}\right); \quad a_1 = a_1^{SST} f_b + (1 - f_b)\, a_1^{REAL} \\
&f_b = \tanh\left[\left(\tfrac{20\cdot\left(c_\mu^{1/4}\Phi + v\right)}{\kappa^2 S\cdot d^2 + 0.01 v}\right)^2\right]; \quad a_1^{SST} = 0.32; \quad a_1^{REAL} = 0.577
\end{aligned} \tag{2.47}$$

Similar to the $k-\omega$ SST model, the blending function f_b is one inside the boundary layer and zero outside.

There are also added length scale limiters in order of avoiding large or small values of the length scale ratio L/L_{vK}, the following limiters are applied:

$$\begin{aligned}
&L_{vK} = \kappa \left|\tfrac{U'}{U''}\right|; \quad |U'| = S; \quad |U''| = \sqrt{\tfrac{\partial^2 U_i}{\partial x_k^2}\tfrac{\partial^2 U_i}{\partial x_j^2}} \\
&L/c_{l1} < L_{vK} < c_{l2}\kappa y; \qquad\quad c_{l1} = 10 \quad c_{l2} = 1.3
\end{aligned} \tag{2.48}$$

A deeper description of the model can be found in [52].

2.4.4 Transition model $\gamma - Re_\theta$

In the majority of today's engineering CFD simulations, the important effect of laminar-turbulent transitions is not included. The reason for this is that transition modeling does not offer the same wide spectrum of CFD-compatible model formulations that are currently available for turbulent flows. There are several reasons for this. First of all, transition occurs by different mechanism in different applications (flow instability bypass transition or separation-induced transition) that are difficult to introduce in just one model. Another reason is that RANS equations do not lend themselves easily to the description of transition flows, where both linear and nonlinear effects are relevant and in RANS equations the effects of linear disturbance growth are eliminated.

There have been some proposals of transition models for CFD computations but they have problems related to cost or compatibility.

The $\gamma - Re_\theta$ transition model fits well with CFD computations and is based on empirical correlations. The central idea of this approach is the Van Driest and Blumer's vorticity Reynolds number that can be used to provide a link between the transition onset Reynolds number from an empirical correlation and the local boundary-layer quantities. It is defined as follows,

$$Re_v = \frac{\rho y^2}{\mu}\left|\frac{\partial u}{\partial y}\right| = \frac{\rho y^2}{\mu} S \tag{2.49}$$

Where y is the distance to the nearest wall.

The maximum value of the vorticity Reynolds number is the momentum-thickness Reynolds number and it is scaled to have a maximum value of one for a Blasius boundary layer.

$$\mathrm{Re}_\theta = \frac{\max\left(\mathrm{Re}_v\right)}{2.193} \tag{2.50}$$

The present transition model is built on a transport equation for intermittency γ, which can be used to trigger transition locally. In addition to the transport equation for the intermittency, a second transport equation is solved for the transition onset momentum-thickness Reynolds number Re_θ. This is required to capture the non-local influence of the turbulence intensity, which changes due to the decay of the turbulence kinetic energy in the freestream, as well as due to changes in the freestream velocity outside the boundary layer.

The transport equation for the intermittency γ is presented in eq. (2.51).

$$\frac{\partial(\rho\gamma)}{\partial t} + \frac{\partial\left(\rho U_j \gamma\right)}{\partial x_j} = P_\gamma - E_\gamma + \frac{\partial}{\partial x_j}\left[\left(\mu + \frac{\mu_t}{\sigma_f}\right)\frac{\partial\gamma}{\partial x_j}\right] \tag{2.51}$$

The transitions sources are defined as follows:

$$P_{\gamma 1} = F_{\text{length}}\, c_{a1}\rho S\left[\gamma F_{\text{onset}}\right]^{0.5}\left(1 - c_{e1}\gamma\right) \tag{2.52}$$

where S is the strain-rate magnitude. F_{length} is an empirical correlation that controls the length of the transition region, and F_{onset} controls the transition onset location. The destruction/relaminarization source is defined as follows:

$$E_\gamma = c_{a2}\rho\Omega\gamma F_{\text{turb}}\left(c_{e2}\gamma - 1\right) \tag{2.53}$$

The transition onset is controlled by the following functions:

$$F_{\text{onset1}} = \frac{\mathrm{Re}_v}{2.193 \cdot \mathrm{Re}_{\theta c}} \tag{2.54}$$

$$F_{\text{onset 2}} = \min\left(\max\left(F_{\text{onset1}}, F_{\text{onset1}}^4\right), 2.0\right) \tag{2.55}$$

$$R_T = \frac{\rho k}{\mu\omega} \tag{2.56}$$

$$F_{\text{onset 3}} = \max\left(1 - \left(\frac{R_T}{2.5}\right)^3, 0\right) \tag{2.57}$$

$$F_{\text{onset}} = \max\left(F_{\text{onset2}} - F_{\text{onset3}}, 0\right) \tag{2.58}$$

$Re_{\theta c}$ is the critical Reynolds number where the intermittency first starts to increase in the boundary layer. This occurs upstream of the transition Reynolds number $\tilde{Re}_{\theta t}$, and the difference between the two must be obtained from an empirical correlation. Both the F_{length} and $Re_{\theta c}$ correlations are functions of $\tilde{Re}_{\theta t}$. The correlations are presented in [53].

The constants for the intermittency equation are:

$$c_{e1} = 1.0; \quad c_{a1} = 2.0 \quad c_{e2} = 50; \quad c_{a2} = 0.06; \quad \sigma_f = 1.0 \tag{2.59}$$

The transport equation for the transition momentum-thickness Reynolds number $\tilde{Re}_{\theta t}$ is presented in eq. (2.60).

$$\frac{\partial\left(\rho\tilde{Re}_{\theta t}\right)}{\partial t} + \frac{\partial\left(\rho U_j \tilde{Re}_{\theta t}\right)}{\partial x_j} = P_{\theta t} + \frac{\partial}{\partial x_j}\left[\sigma_{\theta t}\left(\mu + \mu_t\right)\frac{\partial \tilde{Re}_{\theta t}}{\partial x_j}\right] \tag{2.60}$$

The source term is defined as follows:

$$\begin{gathered} P_{\theta t} = c_{\theta t}\frac{\rho}{t}\left(\mathrm{Re}_{\theta t} - \tilde{Re}_{\theta t}\right)(1.0 - F_{\theta t}) \\ t = \frac{500\mu}{\rho U^2} \end{gathered} \tag{2.61}$$

where t is a time scale, which is present for dimensional reasons.

The blending function $F_{\theta t}$ is used to turn off the source term in the boundary layer and allow the transported scalar $\tilde{Re}_{\theta t}$ to diffuse in from the freestream. $F_{\theta t}$ is equal to zero in the freestream and one in the boundary layer. The $F_{\theta t}$ blending function is defined as follows:

$$F_{\theta t} = \min\left(\max\left(F_{\text{wake}} \cdot e^{-\left(\frac{y}{\delta}\right)^4}, 1.0 - \left(\frac{\gamma - 1/c_{e2}}{1.0 - 1/c_{e2}}\right)^2\right), 1.0\right) \tag{2.62}$$

$$\begin{gathered} \theta_{\mathrm{BL}} = \frac{\tilde{Re}_{\theta t}\mu}{\rho U}; \quad \delta_{\mathrm{BL}} = \frac{15}{2}\theta_{\mathrm{BL}}; \quad \delta = \frac{50\Omega y}{U} \cdot \delta_{\mathrm{BL}} \\ Re_\omega = \frac{\rho\omega y^2}{\mu}; \quad F_{\mathrm{wake}} = e^{-\left(\frac{Re_\omega}{\mathbb{E}+5}\right)^2} \end{gathered} \tag{2.63}$$

The model constants for the $\tilde{Re}_{\theta t}$ equation are

$$c_{\theta t} = 0.03; \quad \sigma_{\theta t} = 2.0 \tag{2.64}$$

The empirical correlation for transition onset is based on the following parameters:

$$\lambda_\theta = \frac{\rho\theta^2}{\mu}\frac{dU}{ds} \tag{2.65}$$

$$Tu = 100\frac{\sqrt{2k/3}}{U} \tag{2.66}$$

Where dU/ds is the acceleration along the streamwise direction. The correlations are presented in [53].

2.5 Verification

Verification studies determine if the results obtained with the numerical methods are reliable. Verification is a mathematical exercise to verify the code and the solution.

There are three errors usually present on numerical calculations: round-off, iterative and discretization error.

The round-off error is due to the finite precision of computers. If double or quadruple precision is used, this error can be considered negligible. This error tends to increase with the grid refinement, but in this thesis all the calculations are done with double precision, so it will be considered negligible.

The iterative error is due to the non-linearity of the equations that are solved.

For steady flows, the iterative error can be studied with the convergence history of the simulation. In this study, the L_2 and L_∞-norm of the non-dimensional residuals of the flow quantities are used to analyze the iterative error.

The L_2-norm is the RMS error over the whole domain of the absolute change of the residuals of a given variable between successive iterations,

$$L_2\left(res_\phi\right) = \sqrt{\frac{\sum_{i=1}^{n_p}\left(\left|res_{\phi_i}\right|^2\right)}{n_p}} \tag{2.67}$$

where res_ϕ is the non-dimensional change of the residual of a given variable, and n_p the total number of grid cells.

The L_∞-norm of the residuals is defined as the maximum absolute change in the whole domain of

the residuals of a given variable between iterations.

The variables analyzed are the three velocity components, the pressure and turbulent quantities as the turbulent kinetic energy k. These quantities are non-dimensionalized using undisturbed flow properties. For the iterative error to be negligible the residuals must be two to three orders below the discretization error, but preferably as low as possible.

Also, apart from the convergence residuals, it is determined if the quantities in study, like C_T or C_P are converged sufficiently. The fluctuation of the quantities are monitored for the last 200 iterations and quantified as a percentage of the final iterative value,

$$U_\phi = 100 \times \max\left(\frac{|\phi_i - \phi_{\text{end}}|}{|\phi_{\text{end}}|}\right), \tag{2.68}$$

The resulting percentage must be at least two to three orders below the discretization uncertainty.

The discretization error usually is the higher order error. It is due to the discretization of the RANS equations to a set of algebraical equations. This error is reduced with grid refinement on steady flows. Doing a refinement study could give insight in the discretization error of the problem.

For steady computations, to study the discretization error the numerical uncertainty U_ϕ of a solution ϕ_i is estimated where the exact solution ϕ_{exact} is unknown. In this thesis, the method described in [54] will be used.

The goal of this study is to define an interval that contains the exact solution with a 95% confidence.

$$\phi_i - U_\phi \leq \phi_{\text{exact}} \leq \phi_i + U_\phi \tag{2.69}$$

The numerical uncertainty for an integral flow quantity ϕ is defined in eq. (2.70).

$$U_\phi = F_s|\varepsilon| \tag{2.70}$$

where F_s is a safety factor and ϵ is the estimated discretization error. This is estimated with Richardson extrapolation (RE), and the discretization error is determined by,

$$\varepsilon \simeq \delta_{RE} = \phi_i - \phi_0 = \alpha h_i^p \tag{2.71}$$

where ϕ_0 is the estimate for the exact solution, ϕ_i represents any integral of local quantity, α is a constant, h is the typical cell size, and p is the observed order of accuracy.

The definition of h is a geometrical problem where a single parameter is used to define the typical cell size of the grids. This requires that the grids must be geometrically similar, which means that the grid refinement ratio must be constant in the complete domain and the grid properties (deviations from orthogonality or skewness) independent of the grid refinement. There are several methods to describe the typical cell size [55].

The typical cell size h_i is defined as the inverse of the number of cells in a grid,

$$h_i = \left(\frac{1}{N_{\text{cells}}}\right)^{\frac{1}{n}} \tag{2.72}$$

where n is the space dimension of the grid (1,2 or 3).

To determine the discretization error ϵ, the determination of ϕ_0, α and p is needed, which are calculated with the least square method using at least four grids. The determination of p is really sensitive to perturbations, so other alternatives to estimate the error are applied, like the ones presented on eqs. (2.73) to (2.75).

$$\delta_{RE}^{02} = \phi_i - \phi_0 = \alpha_{01} h^2 \tag{2.73}$$

$$\delta_{RE}^{12} = \phi_i - \phi_0 = \alpha_{11} h + \alpha_{12} h^2 \tag{2.74}$$

$$\delta_{\Delta_M} = \frac{\Delta_M}{\left(\frac{h_{ng}}{h_1}\right) - 1} \tag{2.75}$$

where $\frac{h_{ng}}{h_1}$ is known as the relative-step size and Δ_M is the data range given by,

$$\Delta_M = \max\left(|\phi_i - \phi_j|\right) \quad 1 \geq i, j \geq n_g, \tag{2.76}$$

where n_g represents the total number of grids. The relative-step size is given by eq. (2.77) for 3-dimensional grids.

$$\frac{h_1}{h_i} = \sqrt[3]{\frac{n_i}{n_1}} \tag{2.77}$$

By using eq. (2.70) and the error estimator ϵ the numerical uncertainty can be obtained. Depending on the value of p the uncertainty can be determined using the following conditions,

- $0.95 \leq p \leq 2.05 : U_\phi = 1.25\delta_{RE} + U_s$
- $p \leq 0.95 : U_\phi = \min\left(1.25\delta_{RE} + U_s, 3\delta^{12}_{RE} + U^{12}_s\right)$
- $p \geq 2.05 : U_\phi = \max\left(1.25\delta_{RE} + U_s, 3\delta^{02}_{RE} + U^{02}_s\right)$
- For oscillatory convergence: $U_\phi = 3\delta_{\Delta_M}$,
- For anomalous behavior: $U_\phi = \min\left(3\delta_{\Delta_M}, 3\delta^{12}_{RE} + U^{12}_s\right)$,

where U_s, U^{02}_s and U^{12}_s are the standard deviations of the least squares fits and 1.25 and 3 represent the safety factors.

3

Numerical Background

Contents

3.1 Numerical tools

The two software used for the numerical calculations are *HEXPRESS* for the grid generation and *ReFRESCO* for RANS computations. This software will be described in this section.

3.1.1 HEXPRESS

In this study, the grids are generated with *HEXPRESS* [56]. This software generates unstructured hexahedral grids automatically and implements hanging nodes for refinements. This software is really easy to use for the user and the amount of time spent is significantly lower compared to the structured grid generator tools [57].

This also has some disadvantages. The quality of the grid is lower, which implies that a higher number of cells is required to obtain an adequate grid quality. Additionally, the grids generated contain hanging nodes that are usually located on the edges where refinement is implemented. These hanging nodes decrease the quality of the mesh due to additional geometric eccentricity.

A number of grid characteristics can be calculated to know if the grid quality is adequate or not. The most important parameters are the orthogonality and the equi-angular skewness, whose expressions are presented on eqs. (3.1) and (3.2) respectively.

$$\text{Orthogonality} \ = 90 - \operatorname{acos}\left(\min\left(\Gamma_{ijk}\right)\right), \tag{3.1}$$

$$\text{Equiangular skewness} \ = \max\left(\frac{(T_{\max} - T_e)}{180 - T_e}, \frac{(T_e - T_{\min})}{T_e}\right), \tag{3.2}$$

$$\Gamma_{ijk} = h_i \cdot (h_j \times h_k), \quad \text{for } i \neq j \neq k \tag{3.3}$$

where T_{min} and T_{max} are the minimum and maximum angle of a face or cell respectively. T_e is the angle of an equiangular face cell, 90 degrees for a quadrilateral face or hexahedral cell. Γ_{ijk} is the mixed product of the unit vectors which link the centroids of two opposite faces of a hexahedral cell, as shown in fig. 3.1.

A good grid to implement ReFRESCO's CFD code should have orthogonality bigger than 10 degrees and an equi-angular skewness lower than 0.9.

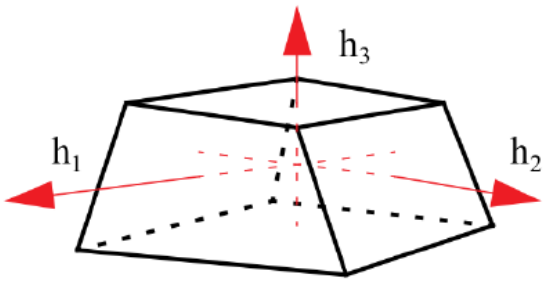

Figure 3.1: Unit vectors used for determination of orthogonality [57]

3.1.2 ReFRESCO

ReFRESCO is a viscous-flow CFD code that solves multiphase (unsteady) incompressible flows with the RANS equations, complemented with turbulence models, cavitation models and volume-fraction transport equations for different phases [58]. A finite-volume approach with cell-centered variables is used to discretize the equations with a strong-conservation form and a pressure-correction equation based on the SIMPLE algorithm to ensure mass conservation [59]. First and second order backwards schemes are used for the time integration where at each time step, the non-linear system of the velocity and pressure is linearized using Picard's method, using a coupled or segregated approach. The coupled linear system is then solved with a matrix-free Krylov subspace method using a SIMPLE-type preconditioner. On the other transport equations a segregated approach is always used. The implementation is face-based. Other CFD features as moving, sliding or deforming grids and automatic grid refinement can be used in the code. For turbulence modelling, RANS/URANS, SAS, DES, PANS and LES approaches can be used. To parallelize the code MPI and subdomain decomposition is used, and runs on Linux workstations and HPC clusters. ReFRESCO is currently being developed, verified and validated at MARIN (in the Netherlands) in collaboration wit IST (in Portugal), USP-TPN (in Brasil), TUDelft (in the Netherlands) and UOS (in UK).

3.2 Discretization of the equations

In eq. (3.4) a general conservation equation for an arbitrary quantity ϕ is presented. The momentum and turbulence equations are solved with this general equation, replacing ϕ with the velocity vector V for the momentum equation or the respective variable for the turbulence equation ($\tilde{\nu}$ for Spalart-Allmaras or k

and $\sqrt{kL}$ for $k-\sqrt{kL}$ model), solving the equation one or two times.

$$\underbrace{\frac{\partial}{\partial t}\int_{\mathcal{V}}\rho\phi d\mathcal{V}}_{\text{Time dependent term}}+\underbrace{\int_{\mathcal{S}}\rho\phi\mathbf{V}\cdot\mathbf{n}d\mathcal{S}}_{\text{Convective term}}=\underbrace{\int_{\mathcal{S}}\Gamma\nabla\phi\cdot\mathbf{n}d\mathcal{S}}_{\text{Dissipation terms}}+\underbrace{\int_{\mathcal{V}}q_{\phi}d\mathcal{V}}_{\text{Source term}} \tag{3.4}$$

In this equation ρ is the density, n the normal outward unit vector, Γ the diffusive coefficient (viscosity μ in case of the momentum equation), and q_ϕ represents a source or sink term. For a steady calculation, the time dependant term disappears.

All this terms are discretized using different methods that will be described next.

3.2.1 Integrals discretization

The integral form of eq. (3.4) contains surface and volume integrals. For the volume integrals, the variable values at the centre of each cells are considered as a proper average for the cell and the integral is discretized as follows,

$$\int_{\mathcal{V}}\phi d\mathcal{V}\approx\phi_c\Delta\mathcal{V} \tag{3.5}$$

where ϕ_c is the integrand value of the variable at the centre of the cell and $\Delta\mathcal{V}$ is the cell volume. On the same way, the surface integrals are discretized as follows,

$$\int_{\mathcal{S}}\phi d\mathcal{S}\approx\sum_{i=1}^{N_f}\phi_{f_i}S_{f_i} \tag{3.6}$$

where ϕ_{f_i} is the integrand value at the surface obtained by interpolation of the neighboring cell center values, S_{f_i} is the face surface of the cell and N_f is the number of faces in the cell. The volume and face surface area of the cell are calculated as described in the next section.

3.2.2 Cell Geometry definition

For each cell volume, the face surface and the location of the center is needed. Consider a three-dimensional polyhedral volume element with N_f cell faces, where every cell face S_f is generated by v line segments N_v that connect the vertices. The face center x_f is calculated by dividing the face surface in $p=N_v-2$ triangles. Each triangle denoted by k_p, consists of three vertices (x_1, x_i and x_{i-1}, with $i=1,2,...,N_v$ and $N_v\geq 3$). The area and the centroid are calculated using eqs. (3.7) and (3.8).

$$A_k = \frac{1}{2} \left| (\mathbf{x}_i - \mathbf{x}_1) \times (\mathbf{x}_{i-1} - \mathbf{x}_1) \right| \tag{3.7}$$

$$\mathrm{x}_k = \frac{1}{3} \left(\mathrm{x}_1 + \mathrm{x}_i + \mathrm{x}_{i-1} \right) \tag{3.8}$$

With fig. 3.2 it can be easier to understand geometrically what has been done to calculate the surface areas and centroid.

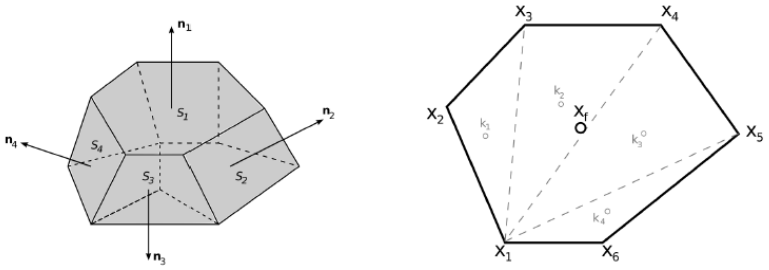

Figure 3.2: Representation of volume element (left) and its face (right) [55]

The face center can now be obtained as the average of the centers of each triangle weighted by the area of the triangle:

$$\mathrm{x}_f = \frac{\sum_{k=1}^{N_k} A_k \mathrm{x}_k}{\sum_{k=1}^{N_k} A_k} = \frac{1}{3} \frac{\sum_{i=3}^{N_v} \left| (\mathrm{x}_i - \mathrm{x}_1) \times (\mathrm{x}_{i-1} - \mathrm{x}_1) \right| (\mathrm{x}_1 + \mathrm{x}_i + \mathrm{x}_{i-1})}{\sum_{i=3}^{N_v} \left| (\mathrm{x}_i - \mathrm{x}_1) \times (\mathrm{x}_{i-1} - \mathrm{x}_1) \right|} \tag{3.9}$$

The surface vector of the cell faces S_f is given by the sum of the triangles areas A_k,

$$S_f = \frac{1}{2} \sum_{i=3}^{N_v} \left| (\mathrm{x}_i - \mathrm{x}_1) \times (\mathrm{x}_{i-1} - \mathrm{x}_1) \right| \tag{3.10}$$

With the magnitude and the location of the face vector, the face unit normal vector can be defined (eq. (3.11)). Using the divergence theorem, the cell volume can be calculated (eq. (3.12)).

$$\mathbf{n}_f = \frac{S_f}{|S_f|}, \quad S_f = \mathbf{n}_f \left| S_f \right| \tag{3.11}$$

$$\Delta \mathcal{V} = \int_{\mathcal{V}} d\mathcal{V} = \frac{1}{3} \int_{\mathcal{V}} \nabla \cdot \mathrm{x} d\mathcal{V} = \frac{1}{3} \int_{\mathcal{S}} \mathrm{x} \cdot \mathrm{n} d\mathcal{S} \approx \frac{1}{3} \sum_{i=1}^{N_f} \mathrm{x}_{f_i} \cdot S_{f_i} \tag{3.12}$$

Finally the location of the cell center is determined as the average of the face centers weighted by the area of each face,

$$\mathbf{x}_c \approx \frac{\sum_{i=1}^{N_f} \mathbf{x}_{f_i} S_{f_i}}{\sum_{i=1}^{N_f} S_{f_i}} \tag{3.13}$$

The next step is to discretize the terms in the integral equations and it will be described in the next sections.

3.2.3 Gradients

For the spatial discretization in eq. (3.4), it is needed to refer to the variables quantities at the cell center and also to the gradients of this quantities. With the divergence theorem, the gradients of an arbitrary quantity ϕ from the cell surfaces can be determined. This theorem is given by eq. (3.14).

$$\int_{\mathcal{V}} \nabla \phi d\mathcal{V} = \int_{\mathcal{S}} \phi \cdot \mathbf{n} d\mathcal{S} \tag{3.14}$$

This leads to eq. (3.15):

$$(\nabla \phi)_c \approx \frac{1}{\Delta \mathcal{V}} \sum_{i=1}^{N_f} \phi_{f_i} \mathcal{S}_{f_i} \tag{3.15}$$

where f_i denotes the specific value at the cell faces i.

3.2.4 Convective terms

The convective term from eq. (3.4) describes the convection of flow property ϕ. For high Reynolds number flows the convective term is much more dominant than the diffusive term, therefore it is of importance that discretization of this term is done while keeping the discretization error as small as possible.

The flow property ϕ and velocity V are needed at the cell faces to discretize the convective term, as well as the face surface S_{fi}. The discretization of the convective term is shown on eq. (3.16).

$$\int_{\mathcal{S}} \rho \phi \mathbf{V} \cdot \mathbf{n} d\mathcal{S} \approx \sum_{i=1}^{N_f} \rho \phi_{f_i} \left(\mathbf{V}_{f_i} \cdot S_{f_i} \right) \tag{3.16}$$

An interpolation to the flow variables at the cell centre must be performed to obtain the flow variables at the cell faces, what is called a convection scheme.

Various convection schemes are available, each with a different level of accuracy, stability conditions and computational efficiency. The four interpolation methods commonly used in CFD codes will be discussed here, as the Central Difference Scheme (CDS), Upwind Difference Scheme (UDS), the blending

scheme, and the Quadratic Upstream Interpolation for Convective Kinematics (QUICK) scheme.

To better understand the different schemes, fig. 3.3 is represented. C_{uu} represents the second upstream cell centroid, C_u the first upstream cell centroid, and C_d the downstream cell centroid. The distance from the cell-centers to the face f is given by S.

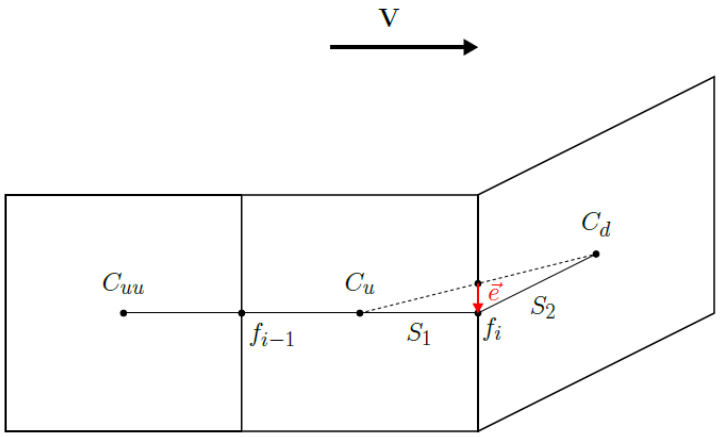

Figure 3.3: Flux representation on a grid [23]

The CDS makes use of the flow variable upwind and downwind from the respective cell-face. The variable value ϕ_{fi} at the face centroid is given by,

$$\phi_{f_i} = \lambda\phi_u + (1-\lambda)\phi_d \tag{3.17}$$

where λ is an interpolation coefficient defined as,

$$\lambda = \frac{S_2}{S_1 + S_2} \tag{3.18}$$

This is based on a Taylor series expansion and it is second order accurate. The UDS method has a first order accuracy, where the face value is given by the value of the face upwind. It is a CDS method with $\lambda = 1$.

$$\phi_{f_i} = \phi_u \tag{3.19}$$

The blending scheme combines this two methods with a blending coefficient β that goes from 0 to 1.

$$\phi_{f_i} = \beta\phi_{f_i}^{CDS} + (1-\beta)\phi_{f_i}^{UDS} \tag{3.20}$$

Finally, the QUICK method is a parabolic interpolation which expression for ϕ_{fi} is defined in eq. (3.21).

$$\phi_{f_i} = \phi_u \lambda \left[S_f^2 \left(\phi_d - \phi_u \right) + S_f \left(1 - S_f \right) \nabla \phi_u \cdot d_{du} \right] \tag{3.21}$$

The four methods discussed are explained extensively in [60].

3.2.5 Diffusive terms

The diffusive term is a surface integral describing the gradient at the surface. The gradient is discretized analogous to the procedure use in section 3.2.4, which results to the following discretization,

$$\int_{\mathcal{S}} \Gamma \nabla \phi \cdot \mathbf{n} d\mathcal{S} \approx \sum_{i=1}^{N_f} \Gamma_{f_i} (\nabla \phi \cdot \mathbf{n})_{f_i} \mathbf{S}_{f_i} \approx \sum_{i=1}^{N_f} \Gamma_{f_i} \left(\nabla \phi_{f_i} \cdot \mathbf{S}_{f_i} \right) \tag{3.22}$$

The gradients at the face centers are needed and ReFRESCO can calculate the gradients either by interpolation of the gradients at the neighboring cell centers (eq. (3.23)), or by dividing the difference of the variable values at the neighboring cell centers by their distance $|d_f|$ (eq. (3.24)).

$$(\nabla \phi)_{f_i} = \alpha_f (\nabla \phi)_{C_u} + (1 - \alpha_f) (\nabla \phi)_{C_d} \tag{3.23}$$

$$(\nabla \phi)_{f_i} = \frac{\phi_{C_d} - \phi_{C_u}}{|d_f|} \tag{3.24}$$

In non-orthogonal grids, the above approaches may compute the gradients in a direction which deviates from the unit normal vector of the cell-face. This difference introduces a constant error which will not vanish with grid refinements. Extra measures have to be taken to reduce this error. ReFRESCO has two types of correction methods which are not discussed here. See [60] for more information.

3.2.6 Source terms

The source term describes the effect of a source q_ϕ in integral form. The source is working on the volume of the cell considered and the integral can therefore be expressed as the source at the cell center multiplied by the volume of the specific cell as shown in eq. (3.25).

$$\int_{\mathcal{V}} q_\phi d\mathcal{V} \approx q_{\phi_c} \Delta \mathcal{V} \tag{3.25}$$

3.2.7 Eccentricity

For the discretization of the governing equations, ReFRESCO needs the integrand values at the cell faces ϕ_f for the surface integrals. Also, variable values at the cell faces are needed to compute gradients at the cell centroid. Usually, ϕ_f is calculated using linear interpolation between two neighboring cell centers and for non-orthogonal grids the position of the computed face variable deviates from the location of the face centroid (see fig. 3.3). This deviation is called eccentricity and can introduce a constant error in the numerical calculations if it is not corrected.

To correct this error, the location of the interpolated value x_e is deviated to the location of the face centroid x_f, which results on an extra term in the calculation of ϕ_f as it is shown in eq. (3.26).

$$\phi_f = \phi_e + (\nabla\phi_e \cdot \mathbf{e}_f) \tag{3.26}$$

where $\mathbf{e}_f$ is the eccentricity vector defined by

$$\mathbf{e}_f = \mathbf{x}_f - [\alpha_f \mathbf{x}_u + (1-\alpha_f)\,\mathbf{x}_d] = \mathbf{x}_f - \mathbf{x}_e \tag{3.27}$$

where α_f is an interpolation factor.

3.3 Solution of the equations

The problem to be solved is a coupled system of equations. There are two methods that ReFRESCO uses to solve this system in its discrete form: coupled and segregated method. The coupled method solves the system of equations for all variables simultaneously while the segregated approach solves each equation for its dominant variable, treating the other values as known. In this thesis, the segregated method is the one used, so the coupled method will not be explained.

The non-linearities and higher-order corrections like the discretized convective term of the momentum equation given by eq. (3.28) needs to be solved iteratively. This process is performed with an outer-loop, which for the convective term results in eq. (3.29).

$$\sum_{i=1}^{N_f} \rho V_{f_i} \left(\mathbf{V}_{f_i} \cdot S_{f_i}\right) \tag{3.28}$$

$$\sum_{i=1}^{N_f} \rho V_{f_i}^k \left(\mathbf{V}_{f_i} \cdot S_{f_i}\right)^{k-1} \tag{3.29}$$

where the subscripts k and $k-1$ represent the current and previous outer loop iterations respectively. The eccentricity and other higher order corrections are also solved in the outer-loop.

After that, a linear system of equations for each variable, the velocity components and the required variables for the turbulence model are solved in a number of inner-loops. Firstly, the three velocity components are determined, then the pressure is corrected (see section 3.32) and finally the turbulence quantities are obtained in one or two extra inner-loops depending on the number of variables of the model. Finally, all this process is repeated that consists in the outer-loop.

To stop the inner- and outer-loops, there are different criterions. It can stop when it reaches a number of iterations determined by the user or when the solution reaches a required level of convergence, looking at the L_2- or L_∞-norm residuals. On fig. 3.4 is presented a schematic of the solution process. More information on the applied solution methods can be found in [61].

3.3.1 Under relaxation

To improve the convergence stability of the solution it is necessary to limit the change in each variable from one outer iteration to the next. A huge change of the variables from one iteration to the next can slow down the process or even prevent from convergence. This limitation in the change is done with under-relaxation. With under-relaxation, the variable to be solved is expressed as a combination between the old and new solution, as shown in eq. (3.30).

$$\phi = \phi^{old} + \beta\left(\phi^{new} - \phi^{old}\right) \tag{3.30}$$

Where β is a variable that can be chosen between 0 and 1. Selecting the correct value for β and thus the amount under-relaxation is largely empirical.

3.3.2 Pressure correction

When the momentum equations are solved sequentially, the set of algebraic equations for each component of the momentum is solved in turn, treating the grid point values of its dominant velocity component

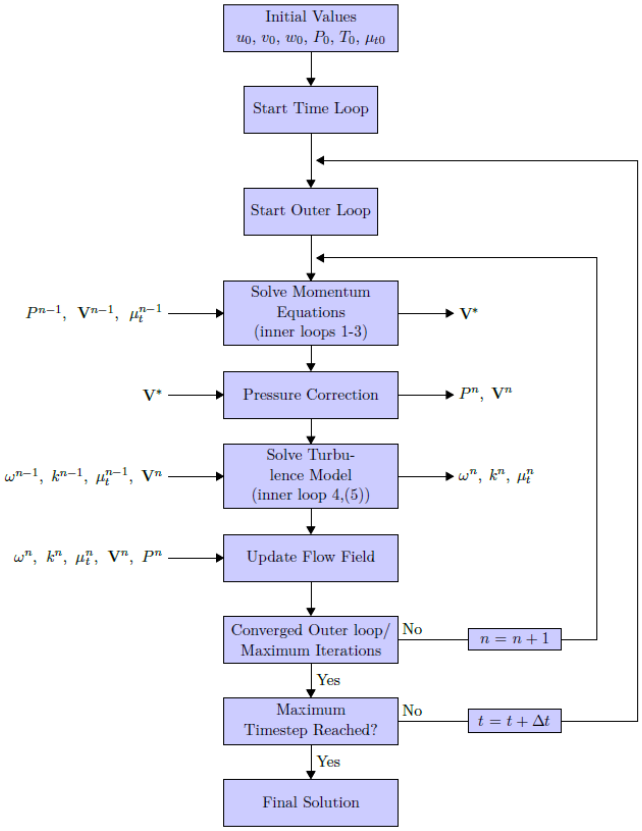

Figure 3.4: Schematic of solution process used by ReFRESCO [23]

as the sole set of unknowns. The pressure field that is used comes from the previous outer loop iteration, so the velocities that are obtained do not normally satisfy the discretized continuity equation. To ensure that, the pressure field needs to be corrected. This is done using the Semi Implicit Method for Pressure Linked Equation (SIMPLE) method that uses the Poisson equation given by eq. (3.31) and consists of three steps:

$$\frac{\partial^2 P}{\partial x_i^2} = -\rho \frac{\partial}{\partial x_i} \left[\frac{\partial \mathbf{V}_j \mathbf{V}_i}{\partial x_j} \right] \tag{3.31}$$

- Step 1: Solve momentum equations using an initial or a previously computed pressure field $\mathbf{P}^{n-1}$. This results in an initial prediction of the velocity field $\mathbf{V}^*$.
- Step 2: Solve the Poisson equation using $\mathbf{V}^*$ to compute the pressure correction $\mathbf{P}'$ at the new iteration step.
- Step 3: Correct the velocity field using the corrected pressure ($\mathbf{P} = \mathbf{P}^{n-1} + \mathbf{P}'$)

4

Numerical Setup

Contents

4.1 Domain

The geometry of the blades of NREL 5MW wind turbine was discussed in section 2.1.1. The hub of the turbine is cylindrical shaped with spherically blunted tangent ogive shaped ends, in order to minimize the curvature variation which may induce flow separation. It has a diameter of 200 mm and a length of 1040 mm at model-scale as shown in fig. 4.1.

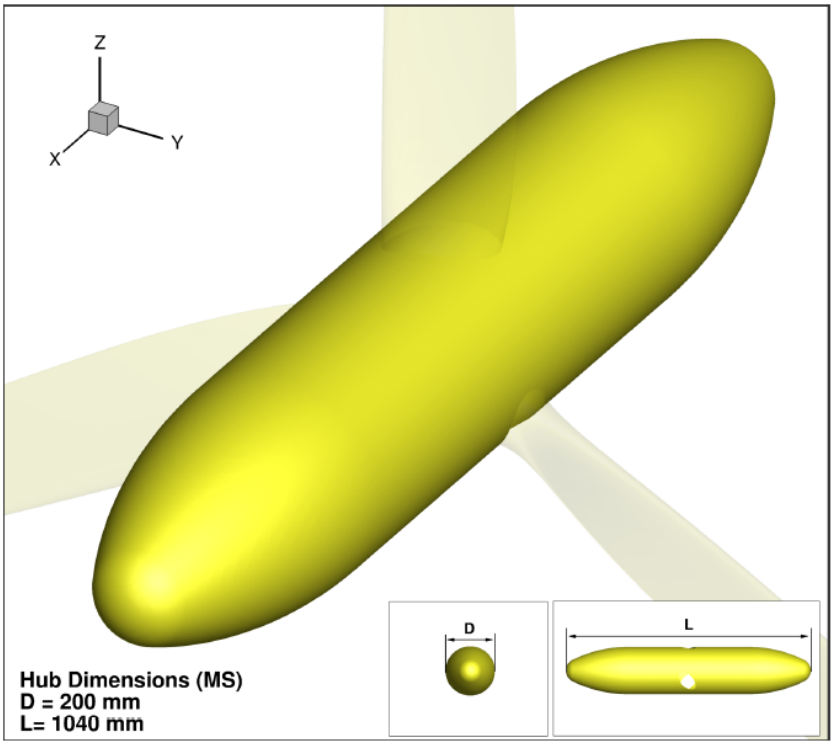

Figure 4.1: Dimensions of the hub at model-scale taken from [23]

The computational domain consists of a cylindrical volume in which the turbine is placed as shown in fig. 4.2. The total length of the cylindrical domain and its radius are defined as a multiple of the turbine diameter. The origin of the coordinate system and the location of the turbine is at 1/5 the length of the cylinder.

4.2 Boundary Conditions

Four boundary conditions are applied to the domain. At the outflow boundary region (B in fig. 4.2) Neumann boundary conditions are applied, where the normal gradients of all quantities are zero as shown

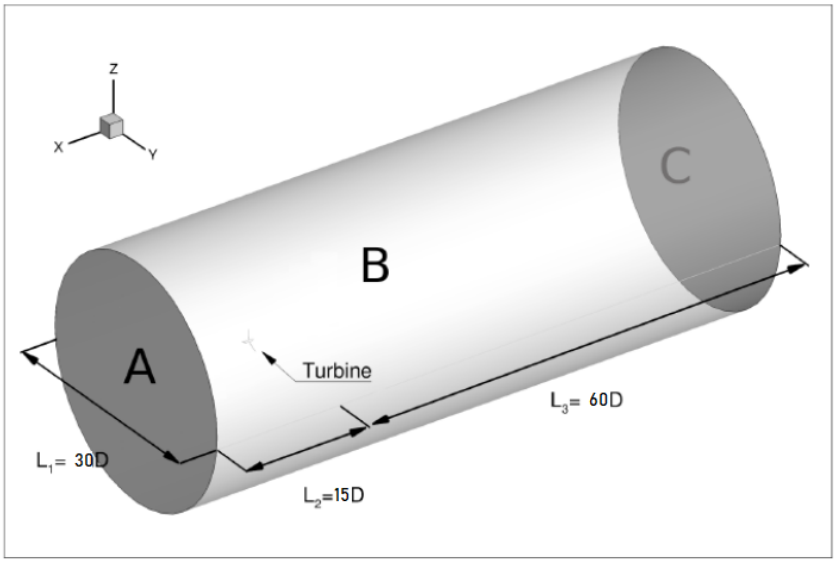

Figure 4.2: Dimensions of the turbine domain taken from [23]

in eq. (4.1).

$$\frac{\partial \mathbf{V}}{\partial \vec{n}} = \frac{\partial p}{\partial \vec{n}} = \frac{\partial k}{\partial \vec{n}} = \frac{\partial \omega}{\partial \vec{n}} = \frac{\partial \gamma}{\partial \vec{n}} = \frac{\partial Re_\theta}{\partial \vec{n}} = 0 \tag{4.1}$$

where $\vec{n}$ is the outward normal unit vector.

A no-slip and impermeability boundary condition is applied at the surface of the turbine. This boundary condition means that it is impossible for the flow to penetrate the surface and, as the flow is viscous, the interaction between the surface and the flow creates a zero velocity at the surface. For the pressure P, intermittency γ and local transition onset momentum thickness Reynolds number Re_θ, Neumann boundary conditions are applied. . In addition, the turbulence kinetic energy k is set equal to zero and ω is specified at the near-wall cell center.

At the inflow boundary region of the domain (A in fig. 4.2), the velocity is set to be the wind velocity, so $\mathbf{V} = (v_{wind}, 0, 0)^T$. The pressure is extrapolated from the interior assuming zero normal derivative (Neumann boundary condition) and the turbulence variables and transition variables are set depending on the model.

The last boundary condition is applied at the wall of the cylindrical domain (B in fig. 4.2). At this wall a pressure boundary condition is applied, which requires the pressure to be constant at the boundary. For the rest of the variables, Neumman boundary conditions are applied.

4.3 Turbine Motion Modelling

Considering the origin x_0 of a non-inertial body-fixed reference frame in which a particle position X is given by,

$$\mathrm{X} = \mathrm{x} + \mathrm{x}_0 \tag{4.2}$$

where x is the position of the particle in the body-fixed frame. With the differentiation of the velocities the following expression can be obtained,

$$\mathbf{V} = \mathbf{U} + \frac{d\mathbf{x}_0}{dt} + \boldsymbol{\Omega} \times \mathbf{x} = \mathbf{U} + \mathbf{V}_g \tag{4.3}$$

$\mathbf{U}$ represents the velocity relative to the body-fixed reference frame, $\frac{d\mathbf{x}_0}{dt}$ the translation velocity and $\boldsymbol{\Omega} \times \mathbf{x}$ the rotation velocity of the body-fixed reference frame itself. The acceleration is given by the total derivative,

$$\frac{D\mathbf{V}}{Dt} = \frac{\mathbf{DU}}{Dt} + \frac{d^2\mathbf{x}_0}{dt^2} + \frac{d\boldsymbol{\Omega}}{dt} \times \mathbf{x} + 2\boldsymbol{\Omega} \times \mathbf{U} + \boldsymbol{\Omega} \times (\boldsymbol{\Omega} \times \mathbf{x}) \tag{4.4}$$

There are five new terms that have to be taken into account for the conservation equations when a non-inertial frame is used. This terms are the acceleration of origin of the non-inertial reference frame, the angular acceleration effect, the Coriolis acceleration, and the centripetal acceleration respectively [62].

There are several methods available to account for the rotative motion, either with inertial or non-inertial frames [62],

- Relative-Formulation (RFM): the RANS equations are written and solved in the moving or relative reference frame. Extra volumic terms, or bodyforces have to be considered.
- Absolute-Formulation (AFM): the RANS equations are solved in the moving reference frame but written in terms of absolute or inertial reference frame quantities.
- Moving-Grid-Formulation (MVG): the RANS equations are written and solved in the earth-fixed reference frame. Due to the motion of the objects, the equations are inherently unsteady, even for steady motions.

The AFM is the method used in this thesis, therefore the additional velocity terms have to be included as well in the governing equations. The integral form of the mass conservation equation then becomes,

$$\int_{\mathcal{S}} (\mathbf{V} - \mathbf{V}_{\mathbf{x}_0}) \cdot \mathbf{n} d\mathcal{S} = 0 \tag{4.5}$$

where $\mathbf{V}_{\mathbf{x}_0}$ us the velocity vector at the origin of the non-inertial body-fixed reference frame, and the momentum equation,

$$\begin{aligned}\int_{\mathcal{S}} \frac{\partial \mathbf{V}}{\partial t} d\mathcal{V} + \int_{\mathcal{S}} \left[\rho \mathbf{V} \left(\mathbf{V} - \mathbf{V}_{\mathbf{x}_0}\right) \cdot n\right] d\mathcal{S} = & \int_{\mathcal{S}} \left(\nu + \nu_t\right) \left[\left(\nabla \mathbf{V} + \nabla \mathbf{V}^T\right)\right] \cdot n d\mathcal{S} + \cdots \\ & - \int_{\mathcal{V}} \nabla \left(p + \frac{2}{3}\rho k\right) d\mathcal{V} + \cdots \\ & - \int_{\mathcal{V}} \rho(\Omega \times \mathbf{V}) d\mathcal{V} + \cdots \\ & + \int_{\mathcal{V}} \rho \mathbf{B} d\mathcal{V}\end{aligned} \tag{4.6}$$

Since all terms are expressed in the inertial reference frame, the boundary conditions are expressed in the inertial reference frame. By using this method, the flow can be solved, in principle, using steady RANS.

4.4 Grid topology

The initial cell size is defined by the turbine diameter. The initial grid is refined toward the geometry of the turbine until a sufficiently refined cell size is obtained at the surface of the turbine blade. Moreover, the grid is refined near the surface of the turbine in order to model properly the viscous layer, based on the dimensionless wall distance y^+ to determine the initial cell size at the turbine surface. To properly model the flow near the wall y^+ typically needs to be below one. The initial size ΔS is determined with eq. (4.7).

$$\Delta S = \frac{y^+ \mu}{\rho V_{fric}} \tag{4.7}$$

where V_{fric} is the frictional velocity at the surface of the turbine.

4.5 Post-processing

The results of the three-dimensional computations consist of the flow field around the turbine including quantities such as velocity, pressure and friction. In addition to these quantities both the forces and moments acting on the turbine blades are calculated. Both the thrust and power coefficients of the turbine can be computed by use of these forces and moments as follows:

$$C_T = \frac{F_x}{\frac{1}{2}\rho V^2 A} \tag{4.8}$$

$$C_P = \frac{M_x \Omega}{\frac{1}{2}\rho V^3 A} \tag{4.9}$$

where Ω is the angular velocity and A the swept area of the turbine given by $A = D^2\pi/4$.

The pressure distribution is expressed by means of the pressure coefficient C_p given by,

$$C_p = \frac{p - p_\infty}{\frac{1}{2}\rho(V^2 + (\Omega r)^2)} \tag{4.10}$$

where V is the air inflow velocity, Ω the angular velocity and r the radius of the turbine.

Another important quantity in order to determine transition is the friction coefficient C_f given by,

$$C_f = \frac{\tau_y}{|\tau_y|} \frac{\sqrt{\tau_x^2 + \tau_y^2 + \tau_z^2}}{\frac{1}{2}\rho V^2} \tag{4.11}$$

where τ_x, τ_y and τ_z are the friction force components. The factor $\frac{\tau_y}{|\tau_y|}$ is used to take into account the direction of the flow.

5

Numerical Study of NREL 5MW

Contents

5.1 Comparison for NREL 5 MW full-scale and model-scale

In this section the RANS computations with ReFRESCO on the full-scale and model-scale NREL 5 MW baseline wind turbine is performed. To scale the wind velocity, Froude-scaling is used as it was discussed before, keeping the geometry the same. An inflow velocity of $V_w = 2m/s$ is used for model-scale conditions while an inflow velocity of $V_w = 14.1m/s$ is used for full-scale conditions. The turbulence model used is the $k-\omega$ SST 2003.

In fig. 5.1 the turbulence viscosity is represented at different sections of the blade for both full-scale and model-scale conditions. With this figure we can clearly see the difference in the flow conditions. At full-scale conditions transition occurs close to the leading edge, which enables the flow to remain attached to the surface when subject to large adverse pressure gradients. For the model-scale, the adverse pressure gradient makes the flow to separate after which transition occurs to the unsteady nature of the flow in the wake-field.

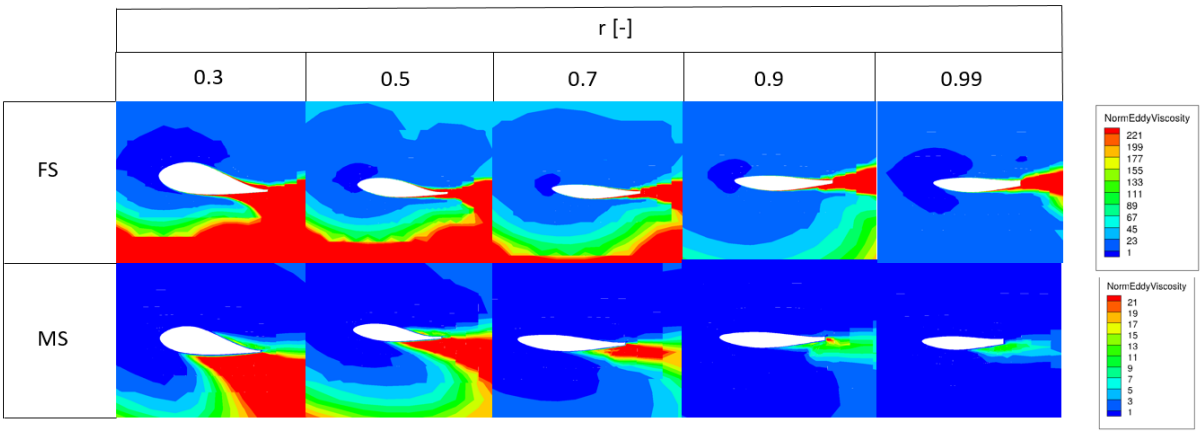

Figure 5.1: Turbulence viscosity at various sections of the blade for full-scale and model-scale NREL 5 MW baseline wind turbine at $TSR = 7.0$

This can also be observed looking at the friction and pressure coefficients for both turbines. On fig. 5.3, the skin-friction coefficient is bigger at model-scale than at full-scale along the blade, as for the full-scale the flow is fully turbulent, while at the model-scale there is transition between laminar and turbulent flow. Skin-friction coefficient is higher for laminar flow. For the pressure coefficient, as shown in fig. 5.2, it is the opposite: it is higher at full-scale than at model-scale along the blade.

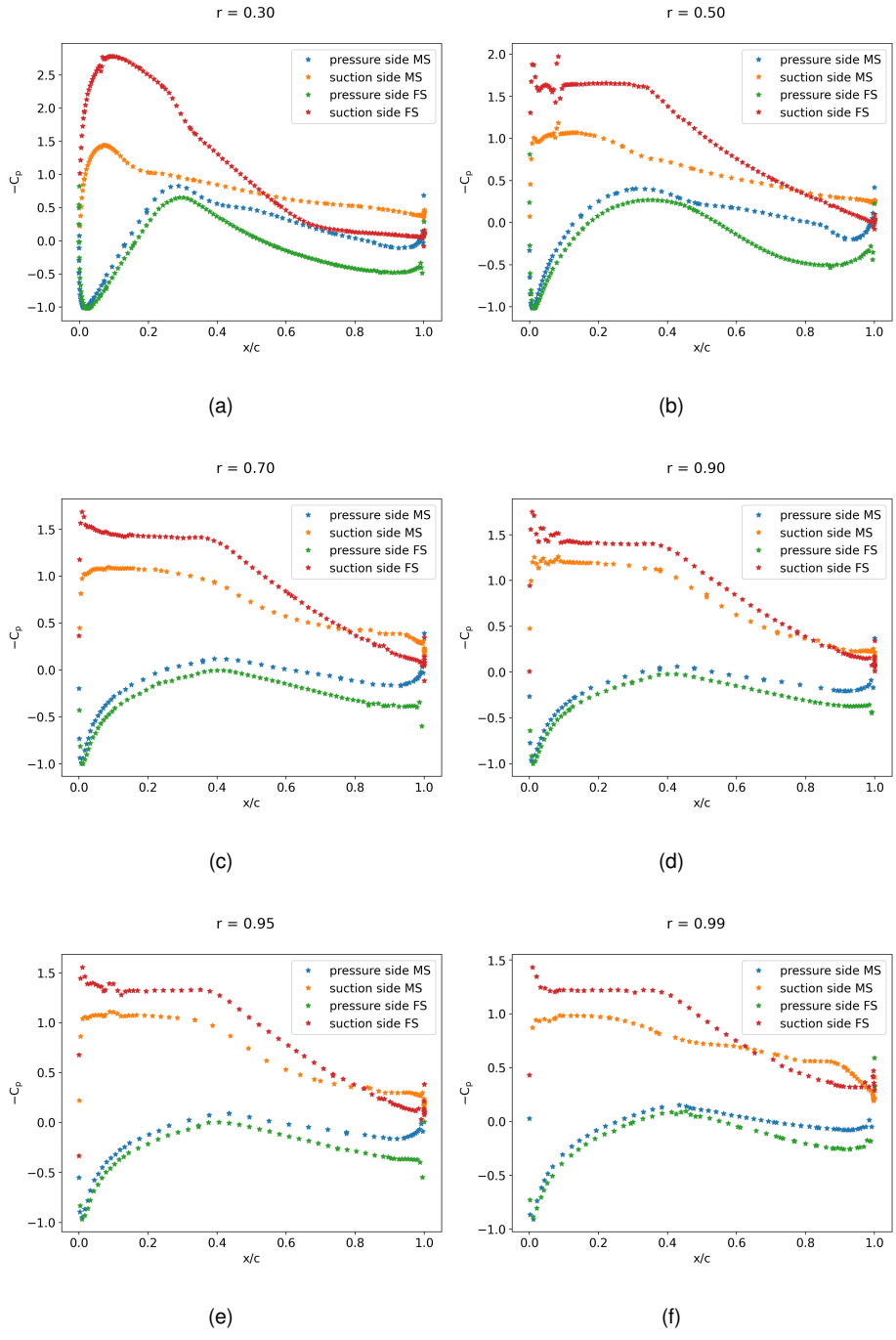

Figure 5.2: C_p at model-scale and full-scale for different blade positions at $TSR = 7$

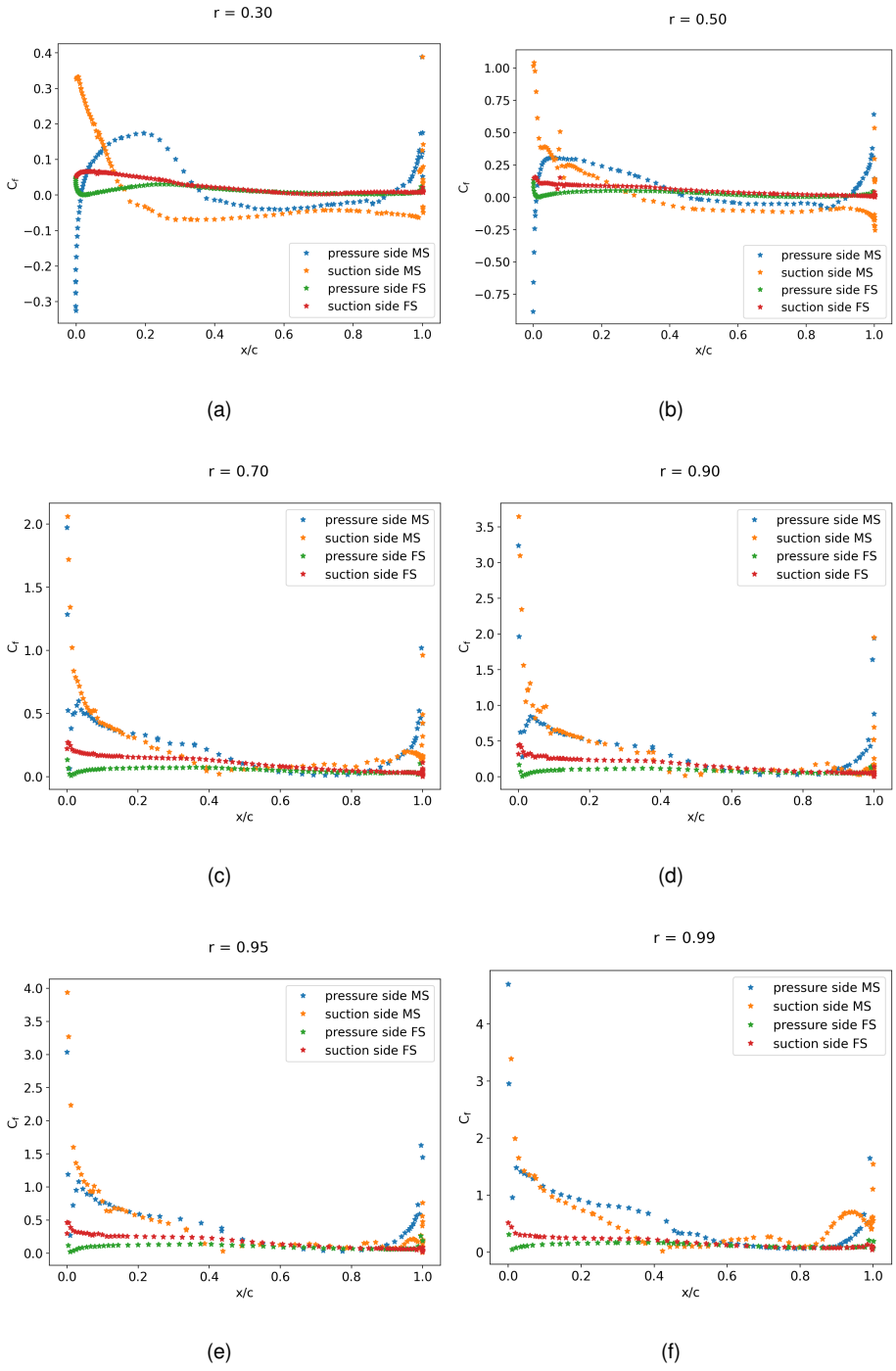

Figure 5.3: C_f at model-scale and full-scale for different blade positions at $TSR = 7$

In fig. 5.4 (a)-(c), the limiting streamlines for model-scale at the suction side of the blade are shown. Due to the laminar character of the flow at model-scale the blade is in stalled condition over the full range of TSRs.

fig. 5.4 (d)-(e), the limiting streamlines for full-scale at the suction side of the blade is presented. In this case, the flow can be considered fully turbulent as the limiting streamlines are on the airflow direction (no attached flow). Separation occurs at low TSRs only due to heavily loaded blades and large local angles of attack.

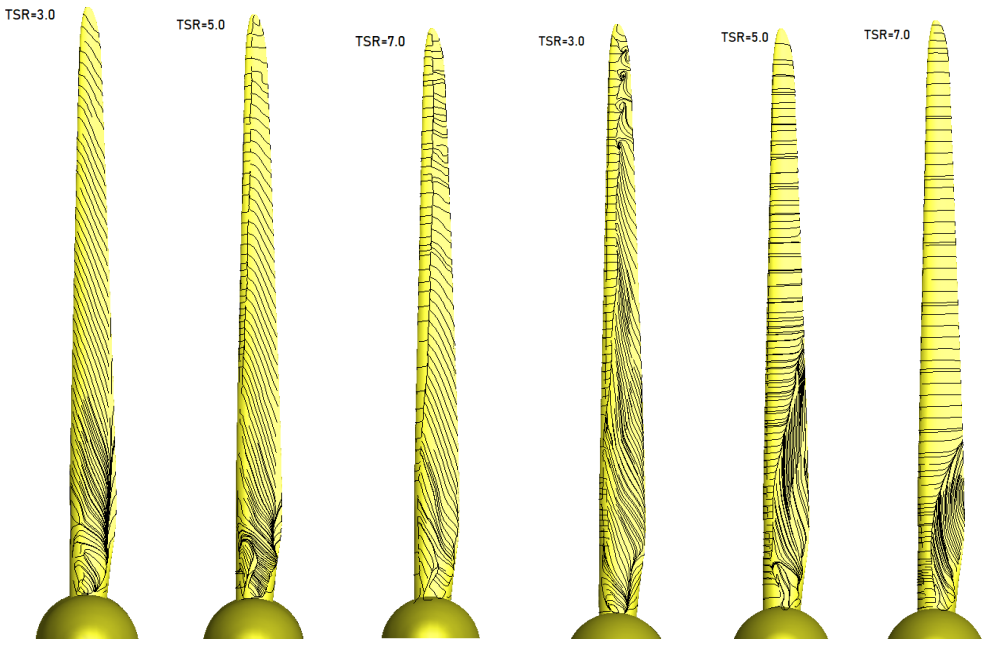

(a) Model (b) Model (c) Model (d) Full (e) Full (f) Full

Figure 5.4: Limiting streamlines for model-scale and full scale NREL 5 MW wind turbine at different TSR

The C_T and C_P at full-scale and model-scale are presented in figs. 5.5 and 5.6 and they are compared with Michel Make's results [23] in order to determine if there is a dramatic change on the results due to the different ReFRESCO versions used for the simulations. Michael Make used version 1.3 back in 2014 while version 2.6 is used on this thesis.

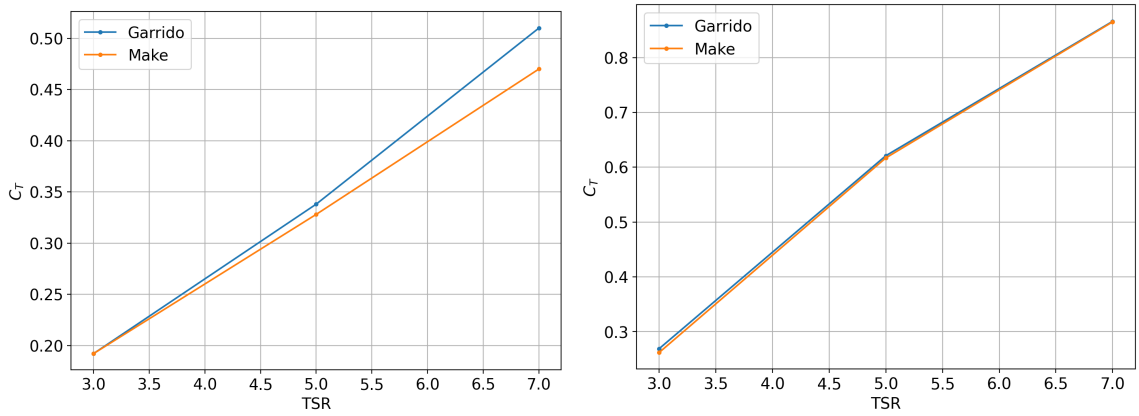

(a) Model-scale (b) Full-scale

Figure 5.5: C_T at model-scale and full-scale for different TSR

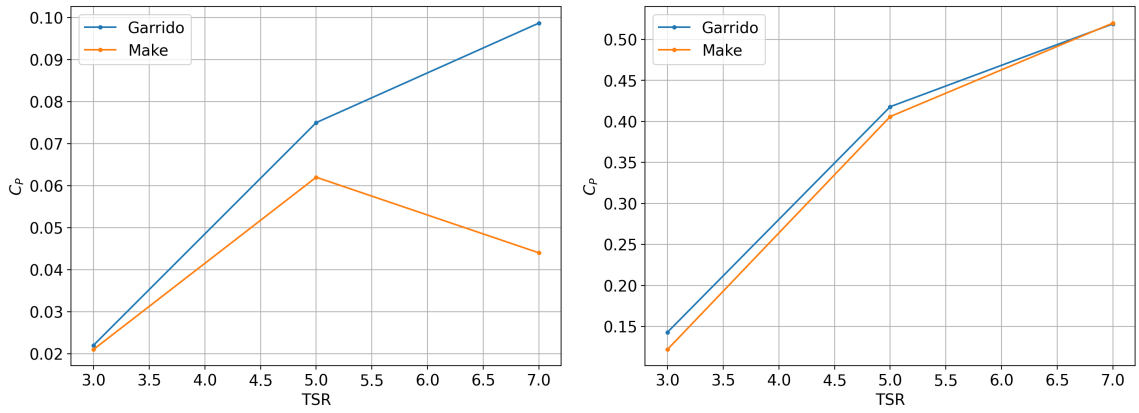

(a) Model-scale (b) Full-scale

Figure 5.6: C_P at model-scale and full-scale for different TSR

As it can be seen, the results calculated with 2.6 and 1.3 versions are really similar for the full-scale turbine while for the model-scale there is a slightly difference for high TSR, that is bigger for the C_P coefficient. C_P is really sensitive to changes.

Comparing this results with the experimental results, it can be observed in fig. 5.7 that, for the experiments, the C_P is negative at model-scale while for the calculations it is positive. Different turbulence models will be tried as well as a transitional model in order to determine which is the best to model the flow.

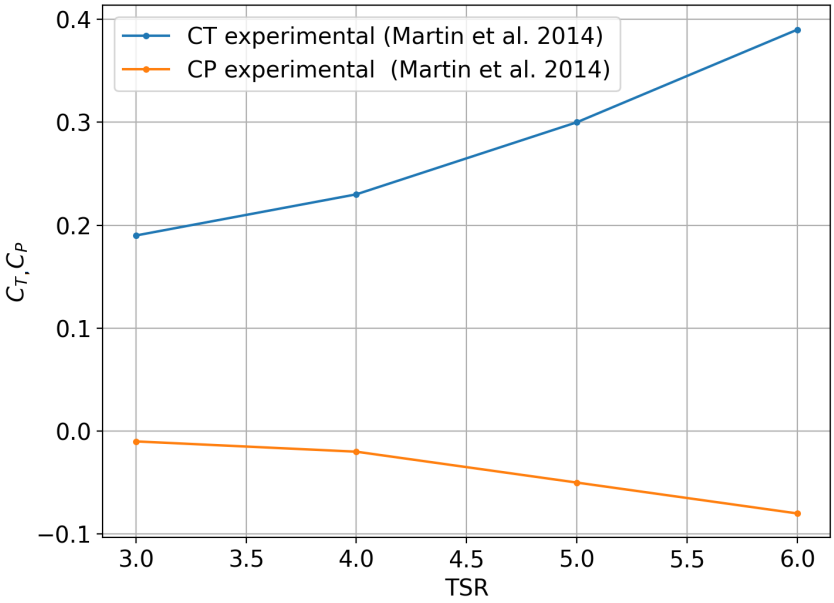

Figure 5.7: Thrust and power coefficients experimental data as function of TSR for model-scale NREL 5MW baseline wind turbine

5.2 NREL 5 MW model-scale at design TSR

This section is focused on the NREL 5 MW model-scale at $TSR = 7$, that it is the design TSR of the turbine. A refinement study will be performed that will follow to a verification procedure, a comparison between three different turbulence models and a transitional model will be used.

5.2.1 Refinement study

In order to determine the numerical uncertainty of the computations, 6 grids are analyzed with the total number of cells varying between $14.3 \cdot 10^6$ and $53.5 \cdot 10^6$. On table 5.1 the properties of the different grids are presented. To generate the grids, the initial size of the grids is changed in HEXPRESS as well as the first layer thickness, in order to maintain geometric similarity as much as possible. The integral quantities C_T and C_P will be used in this analysis.

Table 5.1: Grid properties for the grid refinement study

Grid Refinement	1	2	3	4	5	6	7
Total no. Cells	$14.3 \cdot 10^6$	$17.8 \cdot 10^6$	$19.3 \cdot 10^6$	$25.3 \cdot 10^6$	$29.4 \cdot 10^6$	$37.4 \cdot 10^6$	$53.5 \cdot 10^6$
Minimum Orthogonality	12.6^o	12.8^o	12.3^o	12.2^o	12.0^o	10.3^o	10.9^o
Average Orthogonality	78.9^o	77.9^o	79.8^o	78.4^o	75.8^o	76.4^o	76.1^o
Maximum Skewness	0.88	0.89	0.89	0.89	0.90	0.90	0.91
Grid Ref. Ratio	0.27	0.33	0.36	0.47	0.55	0.7	1.0

5.2.1.A Iterative error

For this iterative error analysis, grid 3 will be used as a sample. The behaviour of the residuals are similar for all seven grids.

On table 5.2 and fig. 5.8 the residuals iterative convergence for grid 3 are presented . The L_2-norm of the residuals are of order 10^{-4}, while for the L_∞-norm the order is around 10^{-1}. A minimum order of 10^{-6} and 10^{-3} for L_2-norm and L_∞-norm respectively is desirable in order to do a verification study. This is not fulfilled in this case. The reason of this could be the unsteady behaviour of the flow at model-scale, specially at the blade root where a vortex is generated as was observed by [22]. The big difference between L_2-norm and L_∞-norm also suggests that the residuals are large only locally, as can be observed on fig. 5.9, where it is shown that the maximum pressure residuals are on the blade root.

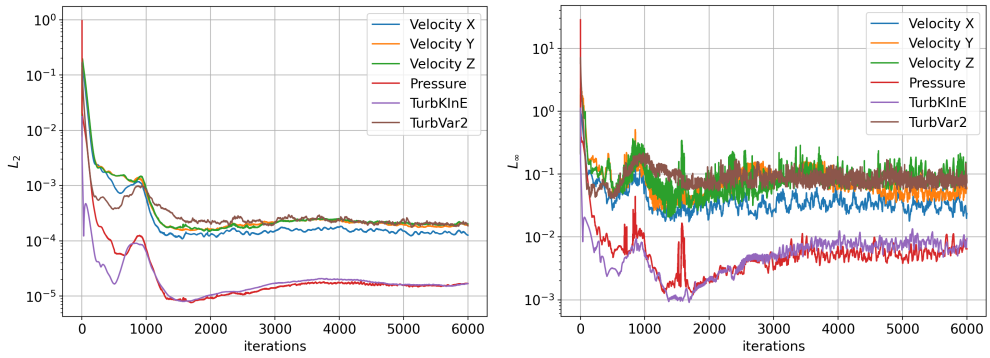

(a) (b)

Figure 5.8: Iterative convergence plots of the L_2-norm and L_∞-norm of the residuals for grid 3

Table 5.2: Iterative convergence and error

Grid Refinement	Total no. Cells	max L_2 residuals	max L_∞ residuals	Fluc. last 200 iterations C_T [%]	Fluc. last 200 iterations C_P [%]
Grid 1	$14.3 \cdot 10^6$	$5.2 \cdot 10^{-4}$	$2.8 \cdot 10^{-1}$	0.001	0.001
Grid 2	$17.8 \cdot 10^6$	$3.6 \cdot 10^{-4}$	$4.2 \cdot 10^{-1}$	0.001	0.001
Grid 3	$19.3 \cdot 10^6$	$2.2 \cdot 10^{-4}$	$3.6 \cdot 10^{-1}$	0.001	0.001
Grid 4	$25.3 \cdot 10^6$	$1.8 \cdot 10^{-4}$	$1.7 \cdot 10^{-1}$	0.001	0.001
Grid 5	$29.4 \cdot 10^6$	$2.1 \cdot 10^{-4}$	$2.2 \cdot 10^{-1}$	0.001	0.001
Grid 6	$37.4 \cdot 10^6$	$1.7 \cdot 10^{-4}$	$3.1 \cdot 10^{-1}$	0.001	0.001
Grid 7	$53.5 \cdot 10^6$	$1.9 \cdot 10^{-4}$	$1.5 \cdot 10^{-1}$	0.001	0.001

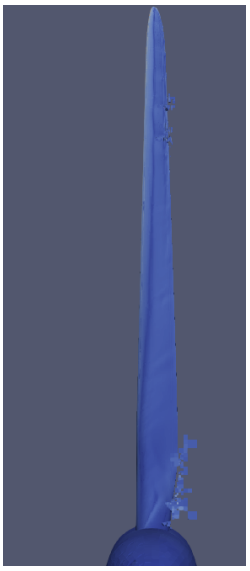

Figure 5.9: Maximum pressure residuals (above 1e-6)

The numerical method used is the steady RANS, which could explain the high residuals. Due to the required computational time, unsteady RANS was not considered but it will be desirable at model-scale conditions due to the unsteady behaviour.

As can be observed in table 5.2, the change after the last 200 iterations on the integrals quantities C_T and C_P is below 10^{-3} percent, which means that despite the large values of the residuals, the integral quantities converge to a constant value. This does not mean that this is the correct value.

In order to be able to neglect the iterative error, the order of convergence must be two to three orders of magnitude below the discretization error. The large iterative error in this case, specially the L_∞-norm, could be too large to be neglected when compared to the discretization error according to the theory presented in 2.5

5.2.1.B Discretization error

The thrust and power coefficients are calculated for the 7 grids in order to determine the discretization error of the computations. In table 5.3 the integral quantities obtained are presented, as well as the numerical uncertainty estimated. As it can be observed, the thrust coefficient and the power coefficient decreases with the number of cells. The power coefficient is more sensitive to the number of cells as it decreases a 62% from the coarsest grid (grid 1) to the most refined grid (grid 7), while for the thrust coefficient the decrease is a 15%. Also, the uncertainty is much higher for C_P than for C_T reaching

350% and 35% respectively. The graphs for the uncertainty estimation are shown in fig. 5.10 for grid 7.

Table 5.3: Power and thrust coefficients for seven different grids

Grid Refinement	C_T	U_ϕ [%]	C_P	U_ϕ [%]
Grid 1	0.57	37	0.16	356
Grid 2	0.54	35	0.14	357
Grid 3	0.54	33	0.13	351
Grid 4	0.52	30	0.10	345
Grid 5	0.51	28	0.09	350
Grid 6	0.50	26	0.08	365
Grid 7	0.48	21	0.06	363

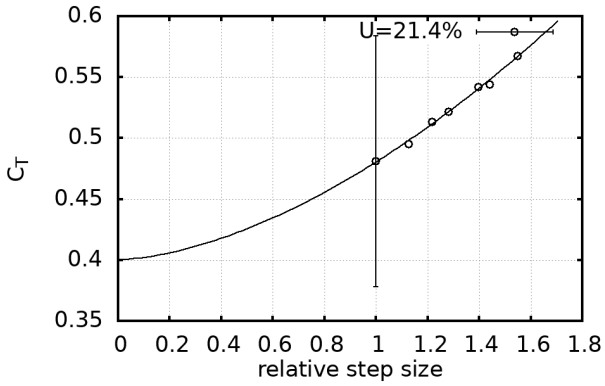

(a)

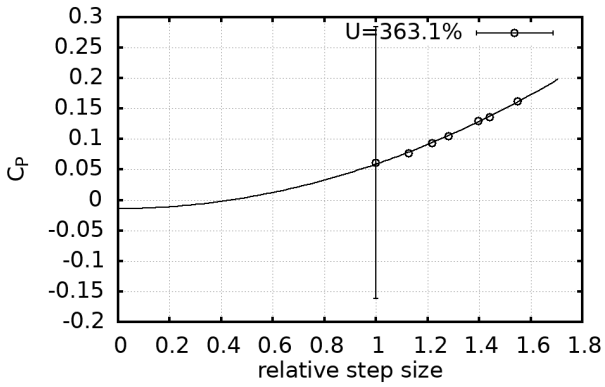

(b)

Figure 5.10: Numerical uncertainty estimation for grid 7

This huge difference between C_T and C_P can be explained with the higher sensitivity to changes in the attached flow region between the computed grids (see fig. 5.11). This is due to the fact that C_P is computed with the moment about the rotating axis of the turbine. As a result of changes in C_l/C_d at the blade tip, C_P is altered significantly due to the distance from the rotating axis. C_T is computed with the axial thrust force, so changes in C_l/C_d along the blade-span contribute equally. The iterative error could

have also affected the uncertainty. Additionally, the fact that C_P has really small values also affects to this uncertainty as a little change represents a large percentage difference.

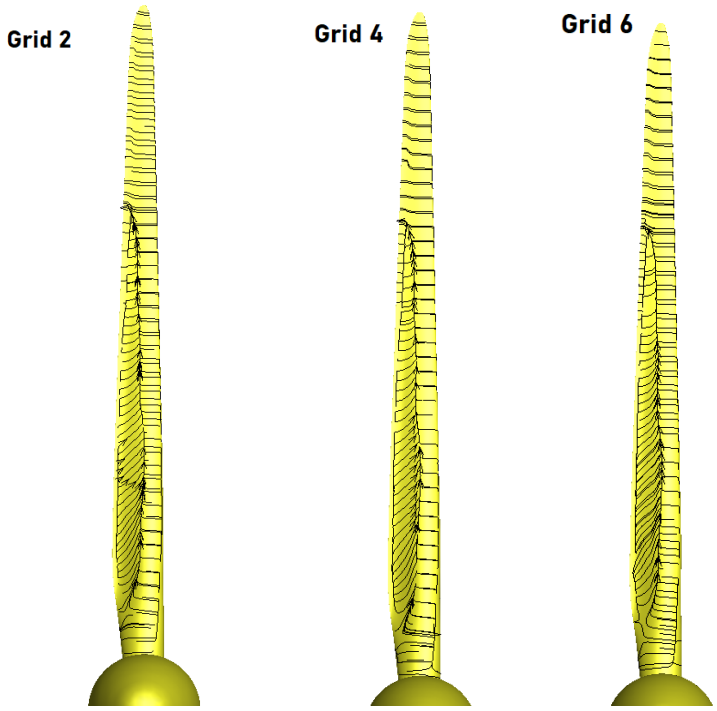

Figure 5.11: Limiting streamlines for different grids

In addition, in fig. 5.12 the iterative convergence of C_T and C_P is presented where the convergence to a constant value can be observed.

5.2.1.C Final remarks

As a conclusion of this study, the challenge of getting appropriate iterative errors using steady calculations for an unsteady flow is observed, which results in large uncertainties especially for the power coefficient.

For the following calculations, grid 4 is the one selected taking into account the computational time needed and that it has the lowest uncertainty for C_P, the variable more affected in the study.

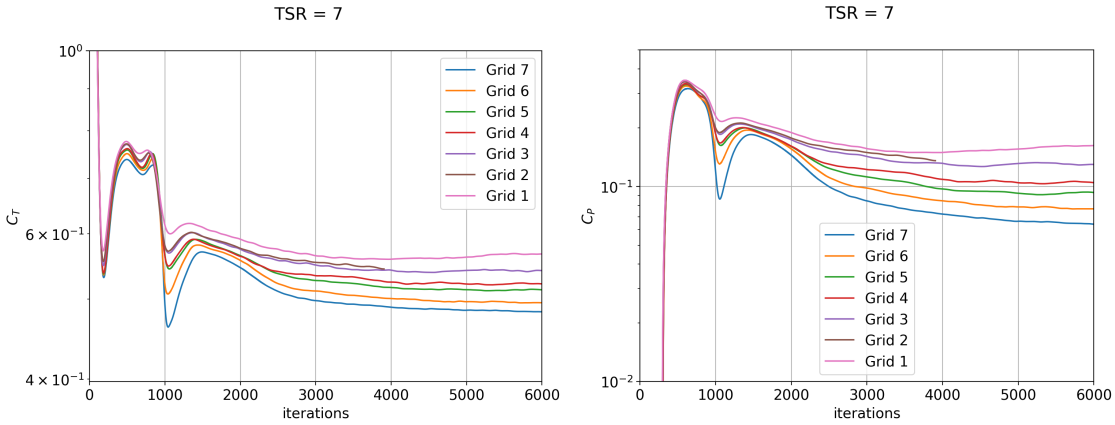

Figure 5.12: Thrust and power coefficients for the different grids

5.2.2 Turbulence modeling

In this section, three different turbulence models are used and compared in order to determine which one is the most suitable to model the flow around the turbine. The models used are the $k-\omega$ SST 2003, Spalart-Allmaras and $k-\sqrt{k}L$. This models are described in section 2.4.3.

This three models are compared for a wind speed of $V_{wind} = 2.0$ m/s. The resulting integral quantities C_T and C_P are presented on fig. 5.13 and table 5.4.

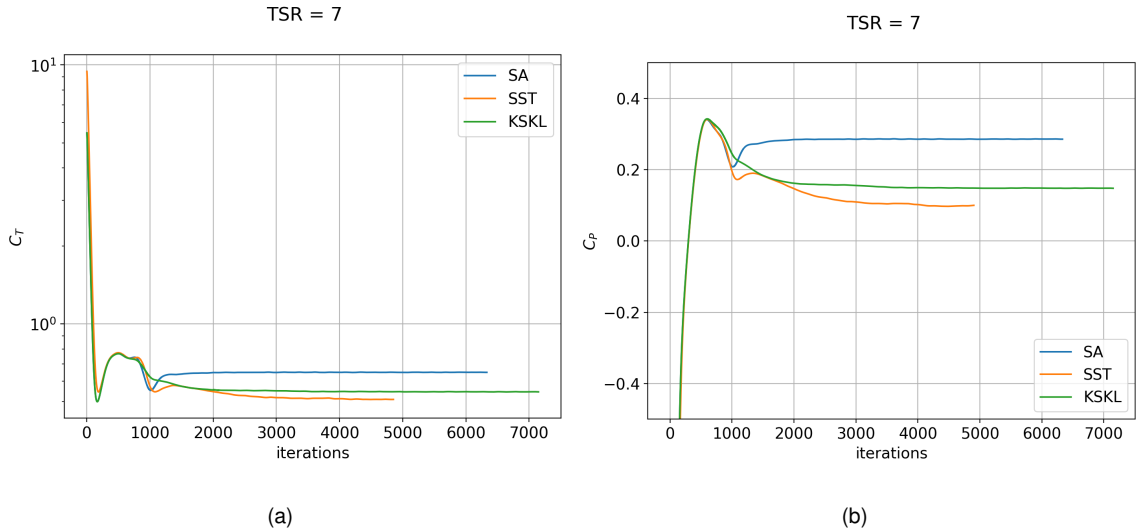

Figure 5.13: Thrust and power coefficients for three turbulence models

Table 5.4: Power and thrust coefficients for three turbulence models

Turbulence Model	C_T	C_P
$k-\omega$ SST 2003	0.511	0.138
Spalart-Allmaras	0.655	0.286
$k-\sqrt{k}L$	0.571	0.148

Analogous to the refinement study the large differences in C_P can be explained to the sensitivity of this quantity with respect to the attached flow region, as it is shown next.

In fig. 5.14 the limiting streamlines for the suction side are shown for the three turbulence models.

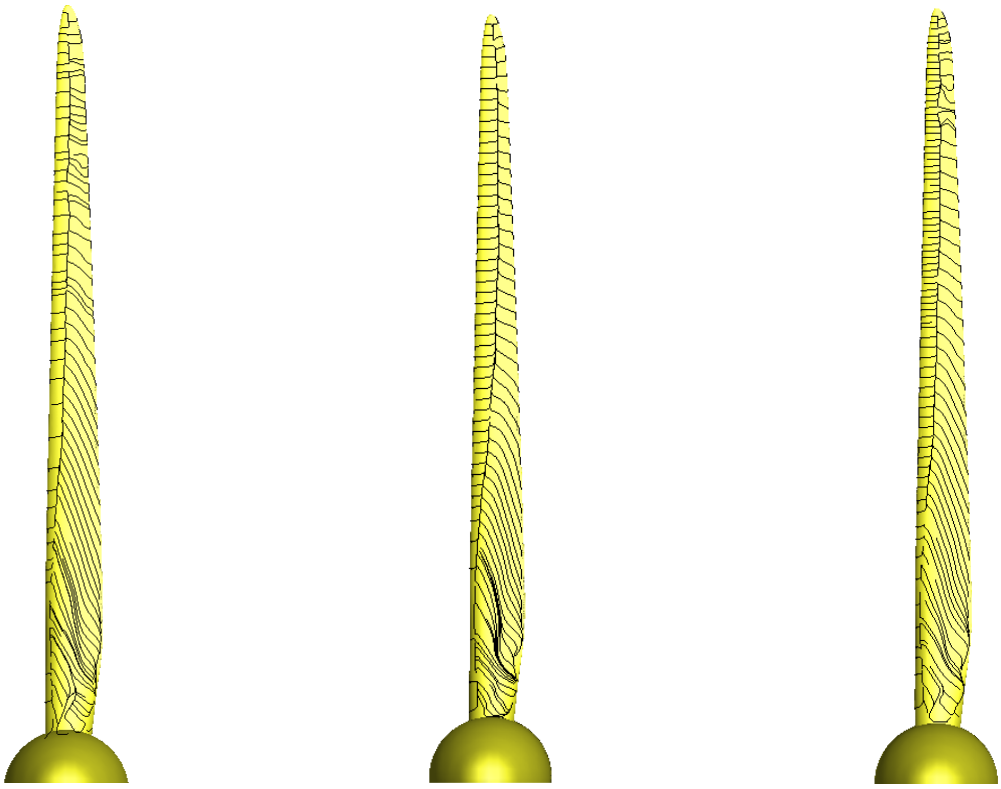

(a) $k-\omega$ SST 2003 (b) Spalart-Allmaras (c) $k-\sqrt{k}L$

Figure 5.14: Limiting streamlines over the suction side of the turbine blades for three turbulence models

For the three models, the flow in the region near the blade tip remains attached. In this region the apparent angle of attack is much smaller than near the root of the blade and the local velocities are higher. As a result the flow is able to remain attached to the surface.

Near the root, the apparent angle of attack is larger and the flow is not longer able to remain attached

to the blade, which causes the separation and the degradation of the performance of the blade locally. The size of the attached region is significantly smaller for the $k-\omega$ SST 2003 model.

The size of the attached region has direct impact on the power coefficient as, for computing it, the torque around the x-axis is used. In the attached region, the lift generated is higher, so this will contribute significantly to the total moment as it is located near the tip of the blade. This explains the big difference in C_p between the models, where the the Spalart-Allmaras model shows a larger attached flow region and C_p value (table 5.4) when compared to the $k-\omega$ SST model and $k-\sqrt{k}L$ model.

The thrust coefficient is computed by the axial force working on the turbine, where lift and drag coefficients over the complete turbine blade span contribute equally, in contrary to the increased contribution of the blade tip with regard to C_P . This leads to a reduction of the sensitivity to the size of the attached flow at the blade tip.

5.2.3 Transition model

The $\gamma - Re_\theta$ transition model explained in section 2.4.4 will be used in order to determine if there is an improvement on the results in comparison with the turbulence models used on the section above. For the transition model, there is a big influence of the turbulence inlet quantities (eddy viscosity ratio $\frac{\mu_t}{\mu}$ and turbulence intensity Tu) on the results of the simulation. The inlet boundary is located 15 diameters upstream from the turbine and a decay of the inlet quantities will occur along the streamwise direction and the values on the turbine will be different from the values at the inlet. To determine which initial values are the ideal ones to model the flow is critical for the simulation. The decay of the turbulence quantities for a uniform flow U are given by the following analytical solutions [63] of the transport equation for k and ω on the $k-\omega$ SST turbulence model:

$$\begin{aligned} k &= k_{\text{inlet}} \left(1 + \frac{\rho\beta k_{\text{inlet}}}{(\mu_{\text{tinlet}}/\mu)\,\mu U}\,(x - x_{\text{inlet}})\right)^{-\beta^*/\beta}, \\ \omega &= \omega_{\text{inlet}} \left(1 + \frac{\rho\epsilon k_{\text{inlet}}}{(\mu_{\text{tinlet}}/\mu)\,\mu U}\,(x - x_{\text{inlet}})\right)^{-1}, \end{aligned} \tag{5.1}$$

where k_{inlet}, ω_{inlet} and x_{inlet} are the values specified at the inlet. The decay of the eddy viscosity ratio is given by,

$$\frac{\mu_t}{\mu} = \frac{\mu_{\text{tinlet}}}{\mu} \left(1 + \frac{\rho\beta k_{\text{inlet}}}{(\mu_{\text{tinlet}}/\mu)\,\mu U}\,(x - x_{\text{inlet}})\right)^{1-\beta^*/\beta} \tag{5.2}$$

while the turbulence intensity is directly related with the kinetic energy by,

$$Tu = 100\sqrt{2k/\left(3U^2\right)} \tag{5.3}$$

These equations show a strong decay for the turbulence quantities. In order to control this decay and get realistic values of the turbulence quantities at the turbine, these quantities will be frozen until one radius in front of the turbine. A sensitivity study will be performed in order to determine which is the pair of values more suitable for the simulation.

A sensitivity study changing the values of the initial eddy viscosity ratio will be done. Three cases will be studied for the eddy viscosity: 2, 10 and 50. The turbulence intensity will be set on 10%. On fig. 5.15 and fig. 5.16 the evolution of the turbulence quantities on the streamwise direction is shown.

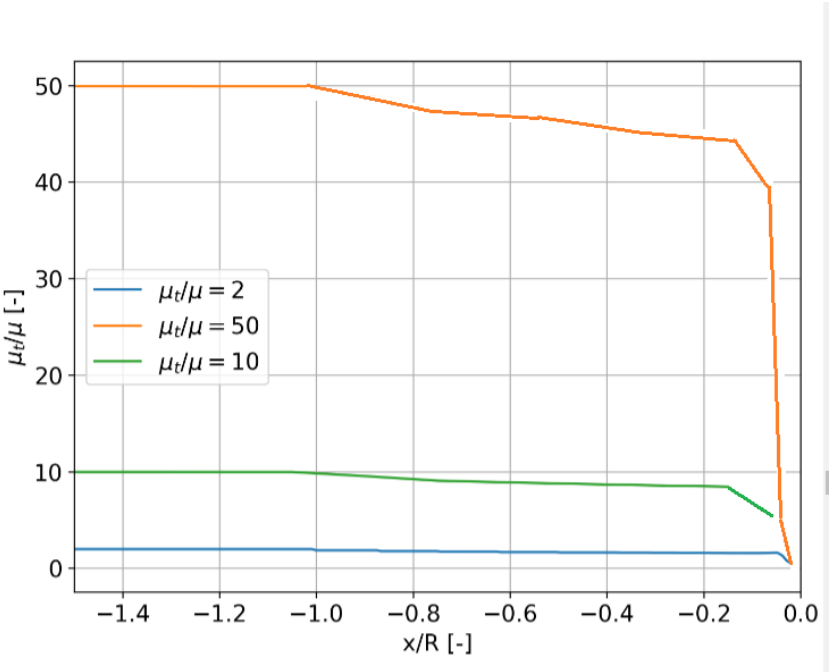

Figure 5.15: Decay of the eddy viscosity ratio along the streamwise direction

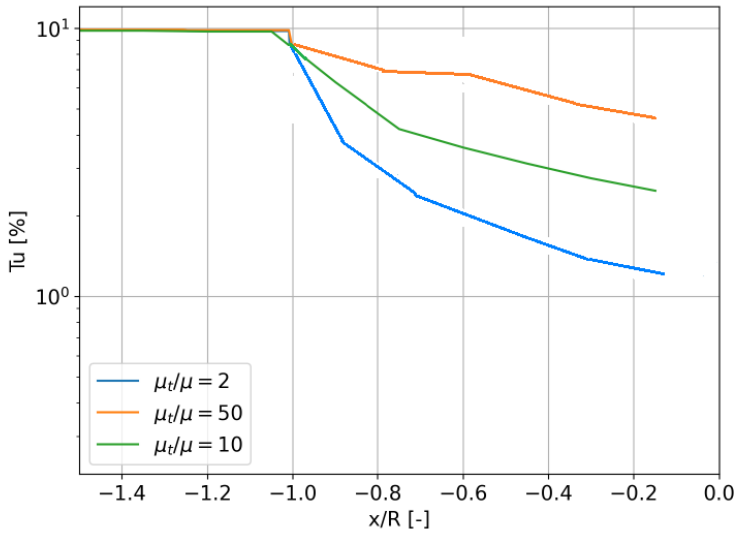

Figure 5.16: Decay of the turbulence intensity along the streamwise direction

A strong decay of the turbulence intensity can be observed on the figure above, while it is less pronounced for the eddy viscosity ratio.

In order to determine if there is a big impact on the results with the eddy viscosity ratio, different parameters will be studied: normalized eddy viscosity contour plots, limiting streamlines, power, thrust, friction and pressure coefficients.

On fig. 5.17 the normalized eddy viscosity contour plots on different sections of the blade are presented for the three cases of eddy viscosity ratio studied.

On fig. 5.18 the limiting streamlines on the suction side of the blades are presented for the three eddy viscosity ratio cases.

Another way of determine transition of the flow in addition to the limiting streamlines is looking at the intermittency γ as it is mention on [64]. If $\gamma > 0.03$ the flow is turbulent while it is laminar if $\gamma < 0.03$. On fig. 5.19, it is shown this condition.

On fig. 5.20 and fig. 5.21 the friction and pressure coefficients at different sections of the blade are presented for the three cases of eddy viscosity ratio studied.

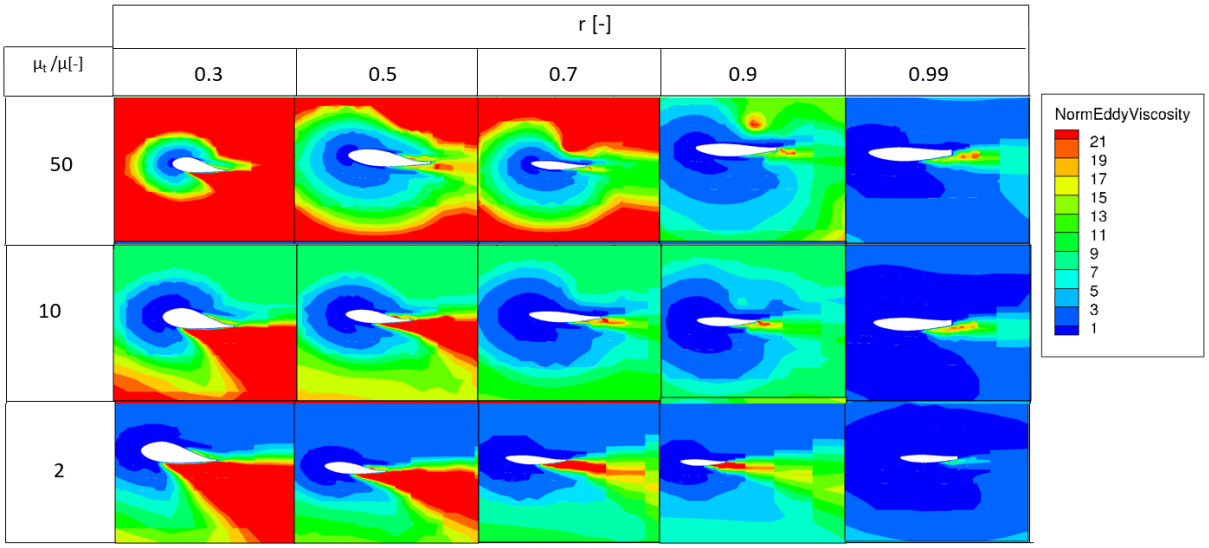

Figure 5.17: Normalized eddy viscosity contour plots on different sections of the blade for the three cases of eddy viscosity ratio

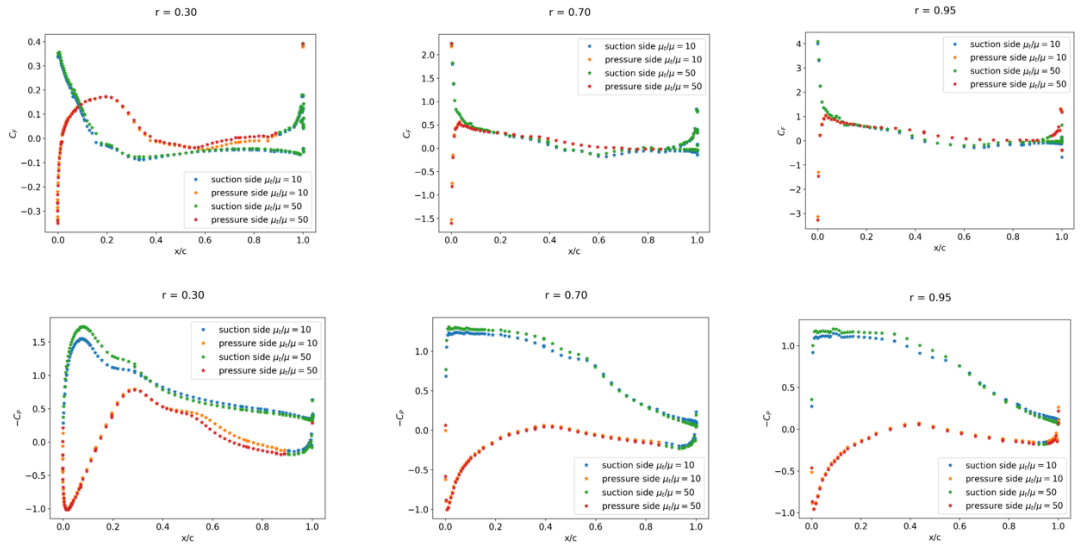

Figure 5.20: Friction and pressure coefficients at different sections of the blade for 10 and 50 eddy viscosity ratio

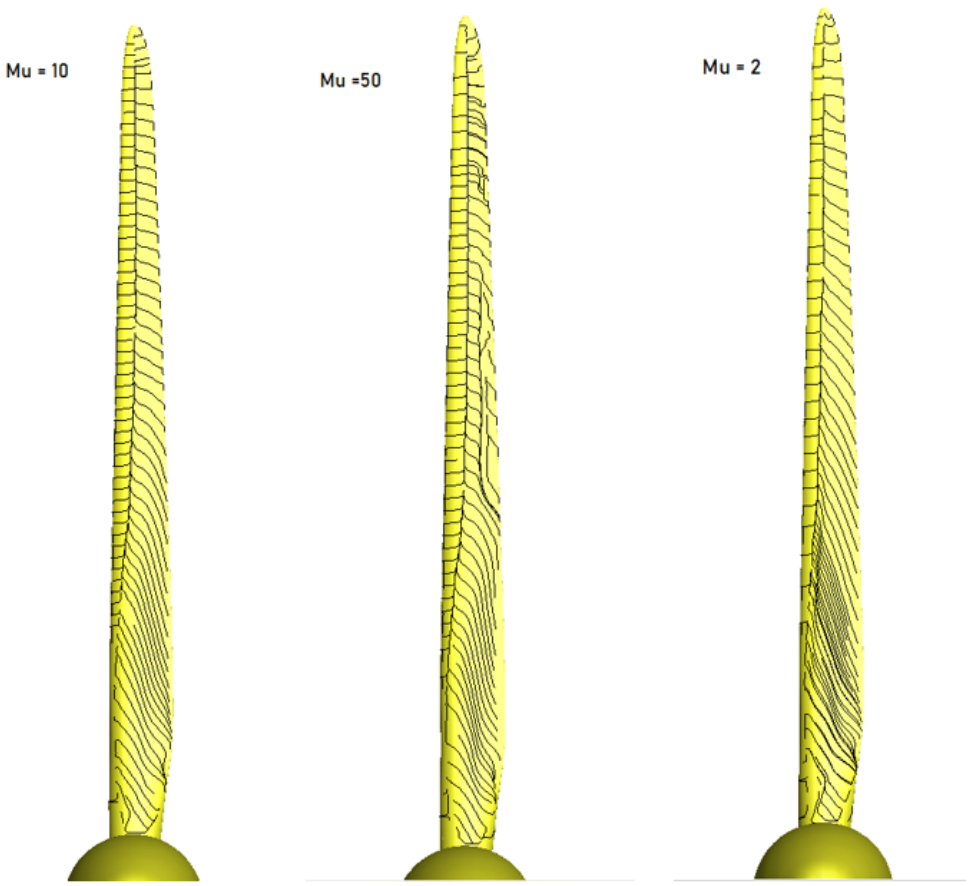

Figure 5.18: Limiting streamlines on the suction side of the blade for the three cases of eddy viscosity ratio

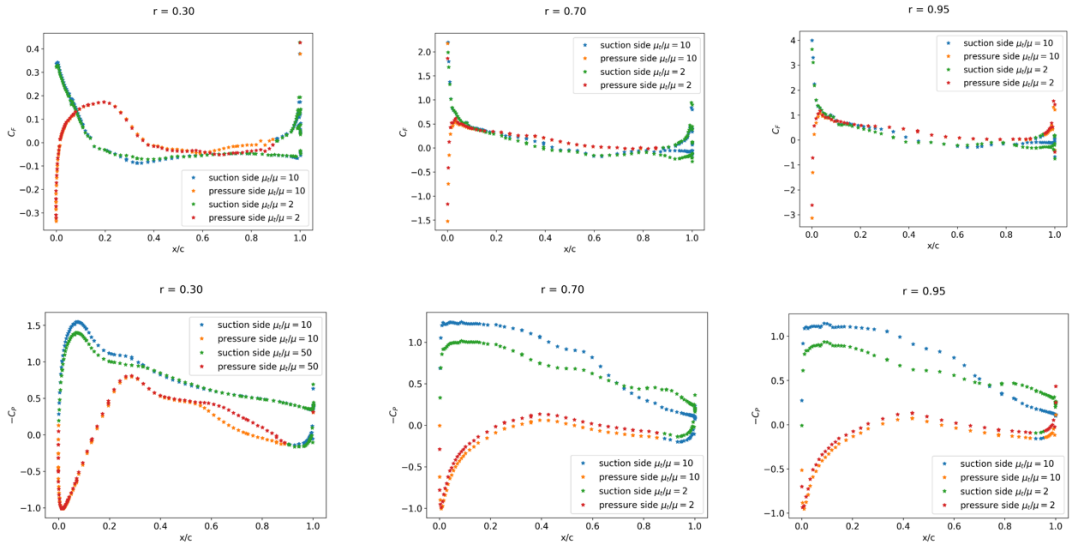

Figure 5.21: Friction and pressure coefficients at different sections of the blade for 10 and 2 eddy viscosity ratio

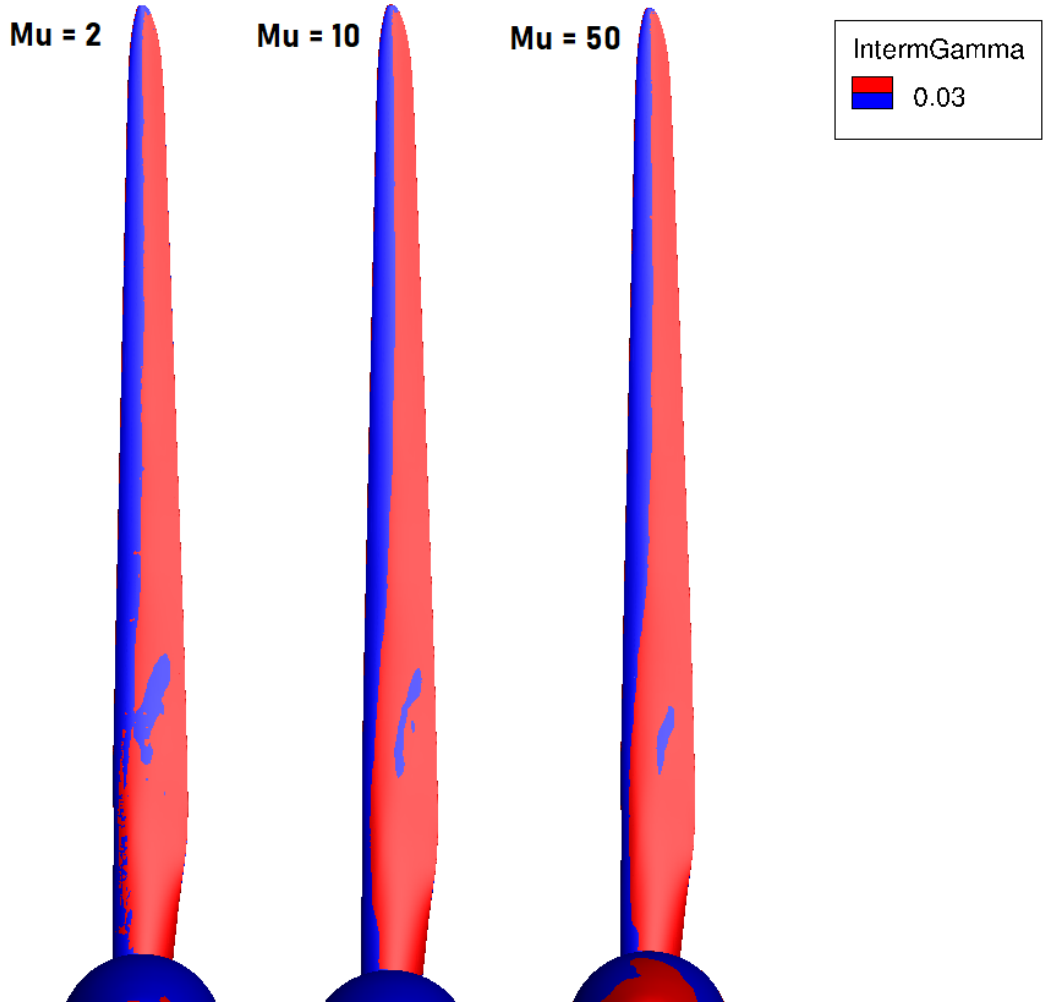

Figure 5.19: γ criterion for visualization of flow separation

Finally, on fig. 5.22 the thrust and power coefficients are presented comparing them with the results for the turbulence models.

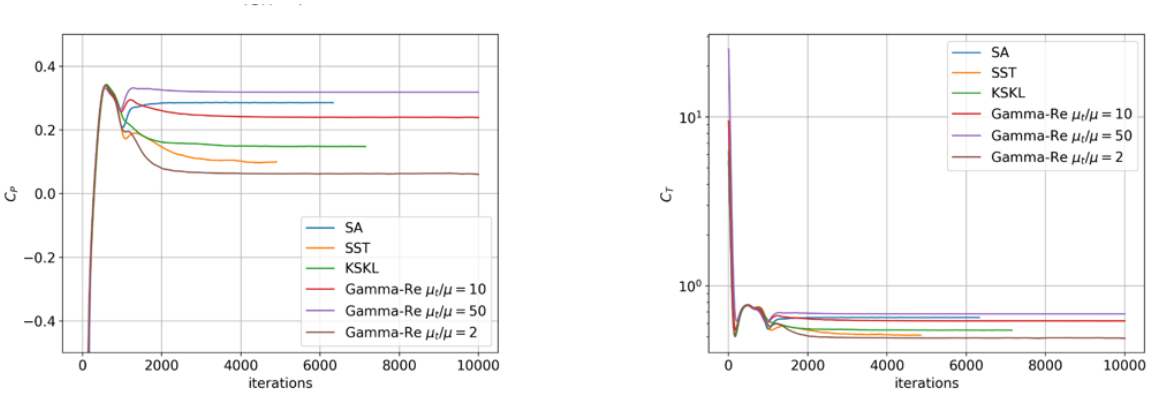

Figure 5.22: Power and thrust coefficients for the transition and turbulence models

Table 5.5: Power and thrust coefficients for transition and turbulence models turbulence models

Turbulence Model	C_T	C_P
$k-\omega$ SST 2003	0.511	0.138
Spalart-Allmaras	0.655	0.286
$k-\sqrt{k}L$	0.571	0.148
$\gamma - Re_\theta$ $\mu_t/\mu = 2$	0.489	0.061
$\gamma - Re_\theta$ $\mu_t/\mu = 10$	0.620	0.239
$\gamma - Re_\theta$ $\mu_t/\mu = 50$	0.683	0.319

As can be observed on the figures, there are differences between the three eddy viscosity ratio cases. As the eddy viscosity increases, the normalized eddy viscosity is bigger around the blade as can be observed on fig. 5.17. Furthermore, as the eddy viscosity ratio increases, the separations occurs before.

Also the friction and pressure coefficients are higher as the eddy viscosity increases as it is shown on figs. 5.20 and 5.21. About the limiting streamlines (fig. 5.18), a difference in the direction followed by them can be also observed . As the eddy viscosity ratio increases, the number of limiting streamlines on the streamwise direction are higher, which means separation of the flow.

The higher difference between the three cases can be observed on the power and thrust coefficients (fig. 5.22). As the eddy viscosity ratio increases, the power and thrust coefficients increases also. Comparing them with the turbulence models, for eddy viscosity ratio 2, the coefficients are the lowest for all the models while for eddy viscosity ratio 50, the coefficients are the highest. The power coefficient is still positive for the three cases in contrast with the negative results of the experiments.

On fig. 5.23 the residuals for turbulence intensity 10% and eddy viscosity ratio 10 are shown in order to observe if there is an improvement with respect to the turbulence models.

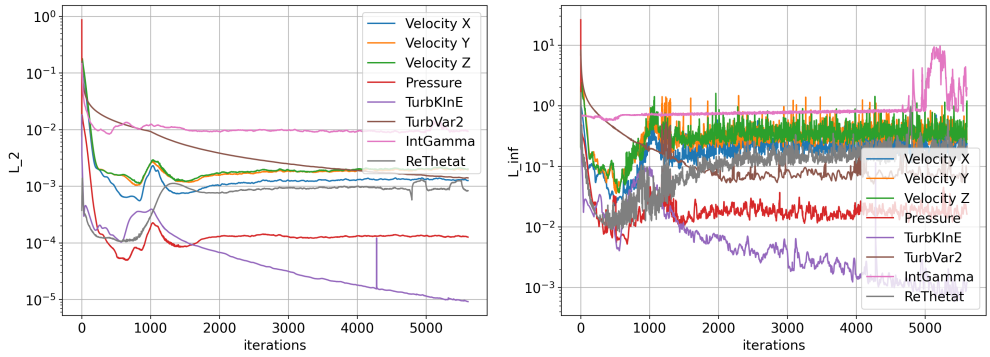

(a) (b)

Figure 5.23: Iterative convergence plots of the L_2-norm and L_∞-norm of the residuals for the transition model

As can be observed, there is not an improvement on the residuals and they are even higher than the turbulence models residuals, especially for the variable γ of this transition model.

As a conclusion, the transition model has not improved the results of the turbulence models but this does not mean that it is not a good option to model this type of turbine with a transition model. Further studies can be done with the transition model in other to achieve the pair of turbulence quantities that best fits with actual behaviour of the flow.

6

Conclusion and recommendations

Contents

6.1 Comparison for NREL 5 MW full-scale and model-scale

First of all, the knowledge obtained from the comparison between the NREL 5MW Wind Turbine at full-scale and model-scale will be summarized:

- The behaviour of the flow around the turbine is different at full-scale and model-scale due to Reynolds dissimilitude that comes from Froude scaling, where aerodynamic forces are not scaled properly. The flow can be considered fully turbulent at full-scale while at model-scale there is transition from laminar to turbulent.
- The different behaviour in the flow causes a poor performance of the NREL 5MW wind turbine at model-scale, specially significant looking at the power coefficient C_P, whose value drops drastically for the full-range of TSRs.
- Friction and pressure coefficients are also affected by the differences on the flow behaviour. Friction coefficient is higher at model-scale than at full-scale along the blade as friction is higher for laminar flow than for turbulent flow. For the pressure coefficient it is the opposite: it is higher at full-scale than at model-scale.

6.2 NREL 5 MW model-scale at design TSR

The knowledge obtained from the NREL 5MW wind turbine at model-scale will be summarized next:

- Large residuals were obtained with the iterative error study performed on different refined grids. The order of the L_2-norm and L_∞ norm residuals obtained was 10^{-4} and 10^{-1}, far from the desirable order, however the integral quantities converged to a constant value. The discretization error obtained was also higher than desirable specially for C_P with uncertainties around 300%, This could be mainly due to the use of a steady RANS at model-scale, where the flow is clearly unsteady.
- Three different turbulence models were used in order to determine which one is the most suitable to model the flow around the turbine at model-scale: $k-\omega$ SST 2003, Spalart-Allmaras and $k-\sqrt{k}L$. Lower values and closer to experimental results for the integral quantities C_T and C_P were obtained for the $k-\omega$ SST model while the higher values were obtained by the Spalart-Allmaras model. This is directly related by the size of the attached region that contributes to the value of the C_P. The size of the attached region for the Spalart-Allmaras model is the higher of the three. However neither of the models replicate the behaviour obtained by the experiments for C_P, where negative values were obtained.

- The transition model $\gamma - Re_\theta$ was used looking for improvements in the results in comparison with the turbulence models, as transition is presented at model-scale. Calibration of the inlet turbulence quantities with transition models. This makes the model difficult to be used for blind predictions of industrial flows. A sensitivity analysis changing the initial values of the eddy viscosity ratio of the flow was performed. The increase of the the eddy viscosity ratio made the separation to occur closer to the leading edge of the blade. Neither the residuals nor the integral quantities improved in comparison to the turbulence models, as the residuals are still higher than desirable and the C_P values are still positive.

6.3 Recommendations for future studies

For future studies, an improvement in the scaling methodology of the NREL 5MW wind turbine should be consider in order to obtain a similar aerodynamic behaviour to the full-scale turbine, that will ease the optimization of it.

It is desirable to perform unsteady RANS (URANS) at model-scale, as the flow is highly unsteady. Lower iterative errors and numerical uncertainties are expected when using URANS and it will give a better understanding of the flow around the turbine.

A deeper study on the transitional model could give the ideal pair of initial turbulence quantities that resemble the real flow around the turbine. As at model-scale there is transition, using this type of models is really promising.

Finally, the study of the coupled problems, with the aerodynamic and hydrodynamic loads acting on the turbine will be the last step to properly model FOWTs and help for optimization.

Bibliography

[1] United Nations. (2020) 2019 Revision of World Population Prospects. [Online]. Available: https://population.un.org/wpp/Download/Standard/Population/

[2] International Energy Agency. (2021) World Energy Outlook 2020. [Online]. Available: https://www.iea.org/reports/world-energy-outlook-2020

[3] Global Wind Energy Council. (2020) Global Wind Report 2019. [Online]. Available: https://gwec.net/global-wind-report-2019/

[4] C. L. Archer and M. Z. Jacobson, "Evolution of global wind power," *Journal of Geophysical Research*, vol. 110, no. D12, 2005.

[5] W. Musial and S. Butterfield, "Future for Offshore Wind Energy in the United States," *Energy Ocean 2004 Conference*, pp. 4–6, 2004.

[6] Global Wind Energy Council. (2020) Global Offshore Wind Report 2020. [Online]. Available: https://gwec.net/global-offshore-wind-report-2020/

[7] J. Jonkman and M. Buhl, "Loads Analysis of a Floating Offshore Wind Turbine Using Fully Coupled Simulation," 2007.

[8] European Wind Energy Association, "Deep Water, The Next Step for Offshore Wind Energy," 2013.

[9] M. N. Schwartz, D. Heimiller, S.Haymes and W. Musial, "Assessment of Offshore Wind Energy Resources for the United States," 2010.

[10] J. Cruz and M. Atcheson, "Floating Offshore Wind Turbines, The Next Generation of Wind Energy," *Green Energy and Technology*, 2016.

[11] H. Dagher, "Making History With VolturnUS," *Webinar Slides University of Maine*, 2013.

[12] CleanTechnica. (2018) Hywind Scotland, World's First Floating Wind Farm, Performing Better Than Expected. [Online]. Available: https://cleantechnica.com/2018/02/16/hywind-scotland-worlds-first-floating-wind-farm-performing-better-expected/

[13] OffshoreWIND. (2020) WindFloat Atlantic Fully Up and Running. [Online]. Available: https://www.offshorewind.biz/2020/07/27/windfloat-atlantic-fully-up-and-running/

[14] J. Jonkman and M. Buhl, "Development and Verification of a Fully Coupled Simulator for Offshore Wind Turbines," *45th AIAA Aerospace Sciences Meeting and Exhibit, 8-11 January, Reno, NV, AIAA Meeting Papers on Disc*, 2007.

[15] Butterfield, C.P.; Musial, W.P.; Simms, D.A. , "Combined Experiment Phase I Final Report. NREL/TP-257-4655. Golden," 1992.

[16] Simms, D.A.; Hand, M.M.; Fingersh, L.J.; Jager, D.W. , "Unsteady Aerodynamics Experiment Phases II-IV: Test Configurations and Available Data Campaigns.NREL/TP-500- 25950. Golden," 1999.

[17] Hand, M.M.; Simms, D.A.; Fingersh, L.J.; Jager, D.W.; Cotrell. J.R., "Unsteady Aerodynamics Experiment Phase V: Test Configurations and Available Data Campaigns. NREL/TP-500-29491. Golden," 2001.

[18] .M.M Hand, D.A. Simms, L.J. Fingersh, D.W. Jager, J.R. Cotrell, S. Schreck and S.M. Larwood, "Unsteady Aerodynamics Experiment Phase VI: Wind tunnel test configurations and available data campaigns. NREL/TP-500-29955," 2001.

[19] H. Snel et al, "The MEXICO project (Model Experiments in Controlled Conditions): The database and first results of data processing and interpretation," 2007.

[20] Schepers, J.G.; Brand, A.J.; Bruining, A.; Graham, J.M.R.; Hand, M.M.; Infield, D.G.; Madsen, H.A.; Paynter, R.J.H.; Simms, D.A. , "Final Report of IEA Annex XIV: Field Rotor Aerodynamics. ECN-C-97-027," 1997.

[21] M. Kretschmer et al, "Effects of Wind Farm Down-Regulation in the Offshore Wind Farm Alpha Ventus," 2019.

[22] E.Ridder et al, "Development of a Scaled-Down Floating Wind Turbine for Offshore Basin Testing," 2014.

[23] M. Make and G. Vaz, "Analyzing scaling effects on offshore wind turbines using CFD," *Renewable Energy 83*, 2015.

[24] K. Boorsma and J.G. Schepers, "New MEXICO experiment, Preliminary overview with initial validation," 2014.

[25] L. G. Salgado, "Experiments in the wind turbine far wake for the evaluation of analytical wake models, MSc Thesis," 2017.

[26] I. Bayati, M. Belloli, L. Bernini, D.M. Boldrin, K. Boorsma, M. Caboni, M. Cormier, R. Mikkelsen, T. Lutz, A. Zasso, "UNAFLOW project: UNsteady Aerodynamics of FLOating Wind turbines," *Journal of Physics: Conference Series*, vol. 1037, no. 7, 2018.

[27] B.Dose et al, "Fluid structure coupled computation of the NREL 5MW Wind turbine blade during standstill," 2019.

[28] Jeon M, et al., "Unsteady aerodynamics of offshore floating wind turbines in platform pitching motion using vortex lattice method," *Renewable Energy*, 2013.

[29] M. Make, G. Vaz et al, "Analysis of aerodynamic performance of floating wind turbines using CFD and BEMT methods," 2015.

[30] H. Yuan et al, "Prediction of the wind turbine performance by using BEM with airfoil data extracted from CFD," *Renewable Energy 70*, 2014.

[31] Erik Prieto S., "Multilevel Panel Method Validation Using the New MEXICO Wind Tunnel Measurements, M.Sc. Thesis," *Renewable Energy 70*, 2017.

[32] Ricardo Balbino Santos Pereira, "Validating the Beddoes-Leishman Dynamic Stall Model in the Horizontal Axis Wind Turbine Environment ," *IST Master Dissertation*, 2010.

[33] A. Korobenko et al, "FSI simulation of two back-to-back wind turbines in atmospheric boundary layer flow," *Computer Fluids 158*, 2017.

[34] S. Lee, M. Churchfield, P. Moriarty, J. Jonkman, and J. Michalakes, "Atmospheric and wake turbulence impacts on wind turbine fatigue loading," 2012.

[35] B. Hand et al, "Numerical simulation of a vertical axis wind turbine airfoil experiencing dynamic stall at high Reynolds numbers," *Computer Fluids 149*, 2017.

[36] Abdulqadir SA et al, "The physical modelling and aerodynamics of turbulent flows around horizontal axis wind turbines," *Energy*, 2016.

[37] N.N. Sorensen et al, "Navier–Stokes Predictions of the NREL Phase VI Rotor in the NASA Ames 80 ft x 120 ft Wind Tunnel," *Wind Energy*, 2002.

[38] N.N. Sorensen, "CFD Modelling of Laminar-turbulent Transition for Airfoils and Rotors Using the $\gamma - Re_\theta$ Model," *Wind Energy*, 2009.

[39] J. M. Jonkman, S. Butterfield, W. Musial, and G. Scott, "Definition of a 5-MW Reference Wind Turbine for Offshore System Development," 2009.

[40] H. R. Martin, “Development of a Scale Model Wind Turbine for Testing of Offshore Floating Wind Turbine Systems,” 2011.

[41] S. Chakrabarti, “Physical Model Testing of Floating Offshore Structures,” *Dynamic Positioning Conf. Model Testing*, pp. 1–33, 1998.

[42] T. Burton, N. Jenkins, D. Sharpe, and E. Bossanyi, *Wind Energy Handbook*, 2011.

[43] J. D. Anderson, *Fundamentals of Aerodynamics*, vol. 5, 2011.

[44] S. J. Miley, *A Catalog of Low Reynolds Number Airfoil Data for Wind Turbine Applications*, 1982.

[45] S. B. Pope, *Turbulent Flows*, 2000.

[46] P. Spalart and S. Allmaras, “A One-Equation Turbulence Model for Aerodynamic Flows,” *AIAA 30th Aerospace Sciences Meeting, Reno, U.S.A.*, 1992.

[47] W. Jones and B. Launder, “The Prediction of Laminarization with a Two-Equation Model of Turbulence,” *International Journal of Heat Mass Transfer*, p. 301–314, 1972.

[48] D. C. Wilcox, *Turbulence Modeling for CFD*, vol. 2, 1988.

[49] F. R. Menter, “Two-Equation Eddy-Viscosity Turbulence Models for Engineering Applications,” *AIAA Journal*, vol. 32, no. 8, 1994.

[50] F. Menter, M. Kuntz, and R. Langtry, “Ten Years of Industrial Experience with the SST Turbulence Model,” *Turbulence, heat and mass transfer*, vol. 4, 2003.

[51] J. C. Rotta, “Statistiche Theorie Nichthomoger Turbulenz,” *Zeitschrift für Physik*, vol. 129, pp. 547–572, 1951.

[52] F. Menter, Y. Egorov, and D. Rush, “Steady and Unsteady Flow Modelling Using the $k-\sqrt{k}L$ Model,” *Heat and Mass transfer*, vol. 5, 2006.

[53] R. B. Langtry and F. R. Menter, “Correlation-Based Transition Modeling for Unstructured Parallelized Computational Fluid Dynamics Codes,” *AIAA Journal*, vol. 47, no. 12, 2009.

[54] L. Eça, G. Vaz, and M. Hoekstra, “Verification and Validation Exercise for the Flow over a Backward Facing Step,” *European conference on computational fluid dynamics*, 2010.

[55] L. Eça, M. Hoekstra, J. Beja Pedro, and J. Falcão de Campos, “On the Characterization of Grid Density in Grid Refinement Studies for Discretization Error Estimation,” 2012.

[56] NUMECA International. (2012) “HEXPRESS Unstructured Full-Hexahedral Meshing.”. [Online]. Available: http://www.numeca.com/en/products/automeshtm/hexpresstm

[57] N. International, *HEXPRESS User Manual*, 2017.

[58] G. Vaz, F. Jaouen, and M. Hoekstra, “Free-surface viscous flow computations. Validation of URANS code fresco,” *28th International Conference on Ocean, Offshore and Arctic Engineering (OMAE)*, 2009.

[59] C. M. Klaij and C. Vuik, “Simple-type preconditioners for cell-centered, colocated finite volume discretization of incompressible reynolds-averaged navier-stokes equations,” *International Journal for Numerical Methods in Fluids*, vol. 71, no. 7, pp. 830–849, 2013.

[60] F. M. S. Pereira, “Verification of ReFRESCO with the Method of Manufactured Solutions,” 2012.

[61] J. H. Ferziger and M. Peric, *Computational Methods for Fluid Dynamics*, vol. 3, 2001.

[62] G. Vaz and D. Rijpkema, “Non-Conformal and Sliding Interfaces in ReFRESCO,” 2013.

[63] P. Spalart, C. Rumsey, “Effective inflow conditions for turbulence models in aerodynamic calculations,” 2007.

[64] B.S. Venkatachary et al., “Assessment of Transition Modeling Capability in OVERFLOW with Emphasis on Swept-Wing Configurations,” 2020.